nature catalysis

Article

https://doi.org/10.1038/s41929-024-01262-w

Parahydrogen-enhanced magnetic resonance identification of intermediates in [Fe]-hydrogenase catalysis

Received: 14 March 2023

Accepted: 30 October 2024

Published online: 13 December 2024

Check for updates

Lukas Kaltschnee[1,2,7], Andrey N. Pravdivtsev[3], Manuel Gehl[4], Gangfeng Huang[4,8], Georgi L. Stoychev[5,6], Christoph Riplinger[6], Maximilian Keitel[1,2], Frank Neese[5,6], Jan-Bernd Hövener[3], Alexander A. Auer[5], Christian Griesinger[1] ✉, Seigo Shima[4] ✉ & Stefan Glöggler[1,2] ✉

Hydrogenases are widespread metalloenzymes used for the activation and production of molecular hydrogen. Understanding the catalytic mechanism of hydrogenases can help to establish industrial (bio)catalytic hydrogen production and conversion. Here we show the observation of so-far undetectable intermediates of [Fe]-hydrogenase in its catalytic cycle. We observed these intermediates by applying a signal-enhancing NMR technique based on parahydrogen. Molecular hydrogen occurs as orthohydrogen or parahydrogen, depending on its nuclear spin state. We found that catalytic conversion of parahydrogen by the [Fe]-hydrogenase leads to notably enhanced NMR signals (parahydrogen-induced polarization, PHIP). The observed signals encode information about how the [Fe]-hydrogenase binds hydrogen during catalysis. Our data support models of the catalytic mechanism that involve the formation of a hydride at the iron centre. Moreover, PHIP enabled studying the binding kinetics. This work demonstrates the hitherto unexploited power of PHIP to study catalytic mechanisms of hydrogenases.

A central challenge in using hydrogen (H_2) as an energy carrier is to find suitable noble metal-free catalysts for efficient H_2 evolution and conversion[1,2]. As an alternative to synthetic noble metal-free catalysts[3,4], hydrogenases, which are widespread in nature[5–7], can perform these tasks with high turnover rates in water and at ambient temperature[8,9]. In addition to their use in electrochemical devices[10], hydrogenases can also be used in suitable microorganisms, coupling H_2 evolution or conversion to fermentation[11,12] or photosynthesis[13–19].

Hydrogenases are grouped into three different evolutionary types, that is, [NiFe]-, [FeFe]- and [Fe]-hydrogenases[5,20]. While intermediates in the catalytic cycle of [NiFe]- and [FeFe]-hydrogenases have been studied by Fourier transform infrared spectroscopy[21,22], electron paramagnetic resonance[23,24], high-resolution X-ray diffraction[25], nuclear resonance vibrational spectroscopy[26,27] and nuclear magnetic resonance spectroscopy (NMR)[28], intermediates of the catalytic cycle of [Fe]-hydrogenases were thus far undetectable. [Fe]-hydrogenases

[1]Max-Planck Institute for Multidisciplinary Sciences, Göttingen, Germany. [2]Center for Biostructural Imaging of Neurodegeneration, Göttingen, Germany. [3]Section Biomedical Imaging, Molecular Imaging North Competence Center, Department of Radiology and Neuroradiology, University Medical Center Schleswig–Holstein, Kiel University, Kiel, Germany. [4]Max-Planck Institute for Terrestrial Microbiology, Marburg, Germany. [5]Max-Planck Institut für Kohlenforschung, Mühlheim an der Ruhr, Germany. [6]FAccTs GmbH, Köln, Germany. [7]Present address: Clemens-Schöpf-Institute for Organic Chemistry and Biochemistry, Technical University Darmstadt, Darmstadt, Germany. [8]Present address: Institute of Analytical Chemistry and Instrument for Life Science, The Key Laboratory of Biomedical Information Engineering of Ministry of Education, School of Life Science and Technology, Xi'an Jiaotong University, Xi'an, China. ✉e-mail: cigr@mpinat.mpg.de; shima@mpi-marburg.mpg.de; stefan.gloeggler@mpinat.mpg.de

https://doi.org/10.1038/s41929-024-01262-w

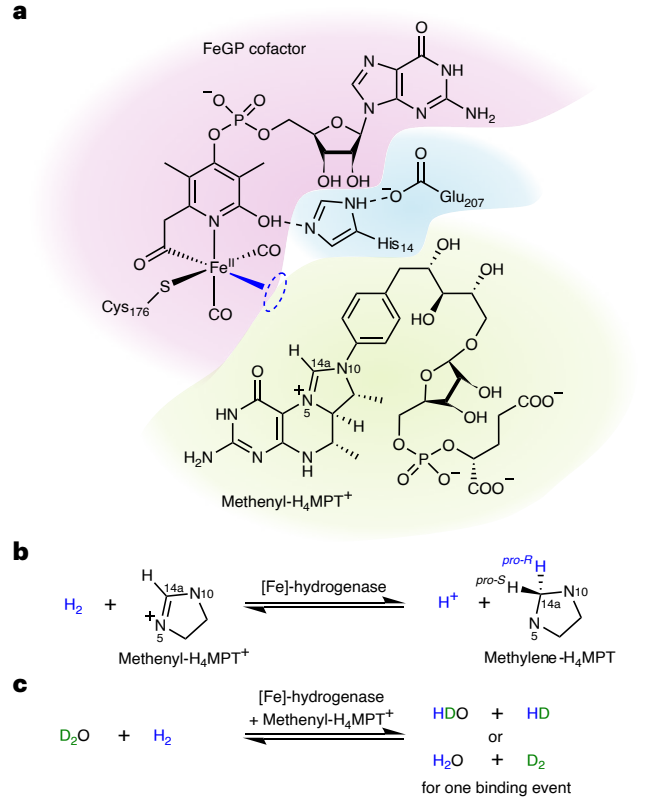

Fig. 1 | Active site of Hmd and reactions catalysed by Hmd. a, The FeGP cofactor (magenta) and methenyl-H_4MPT^+ substrate (green) in the closed active site. The proposed H_2 binding site is highlighted in blue, and the hydride acceptor C_{14a} is marked in methenyl-H_4MPT^+. His14 and Glu207 mark the start of the putative proton relay network[29], highlighted in light blue. **b**, Methenyl-H_4MPT^+ reduction reaction, catalysed by Hmd with hydride transfer[20,32]. For methenyl-H_4MPT^+ and methylene-H_4MPT, only the imidazolinium and imidazolidine rings are depicted. **c**, Hydrogen/deuteron isotope exchange reaction, catalysed by Hmd[33].

contain a single iron atom at the active site that maintains the diamagnetic Fe^{+II} state throughout the catalytic cycle[29]. The iron is complexed in an iron-guanylyl pyridinol (FeGP) cofactor (Fig. 1a, magenta)[29–31]. Upon binding of the substrate methenyl-tetrahydromethanopterin (methenyl-H_4MPT^+, also CH≡H_4MPT^+) (Fig. 1a, green), the protein changes from an open to a closed conformation, thereby bringing together FeGP and CH≡H_4MPT^+ to form the active site (Fig. 1a). In the active site, H_2 is heterolytically cleaved ($H_2 \rightleftarrows H^+ + H^-$) and the hydride ($H^-$) is stereo-specifically transferred to the $H_{pro\text{-}R}$ position of the methylene carbon (C_{14a}) of methylene-H_4MPT (CH_2=H_4MPT) (Fig. 1b)[32]. Owing to this heterolytic reaction, [Fe]-hydrogenase is also referred to as H_2-forming methylene-H_4MPT dehydrogenase (Hmd). Hmd catalyses isotope exchange between water and dissolved hydrogen, where both single- and double-isotope exchange can take place in one binding event (Fig. 1c)[33]. Computational models suggest multiple iron hydrogen species along the Hmd catalytic cycle[29,34,35]. However, none of these species have yet been characterized experimentally[29–32,36–39].

To characterize these bound hydrogen species, we studied Hmd using sensitivity-enhanced NMR based on parahydrogen (p-H_2). p-H_2 stands for H_2 that is enriched in its antisymmetric nuclear spin state, the para-state. Upon contact with a H_2-activating catalyst, p-H_2 can create strong NMR signals via parahydrogen-induced polarization (PHIP) effects[40–44]. Thereby, PHIP effects make it possible to characterize transiently bound hydrogen species with strongly enhanced sensitivity[45–50]. We demonstrate that PHIP can be used to study the H_2 catalysis of metalloenzymes.

Results and discussion

Identification of enhancement effects on reaction products

We first observed ^{1}H-NMR signals that transiently appear after treating solutions of reconstituted Hmd holoenzyme from *Methanocaldococcus jannaschii* (jHmd) and its substrate (methenyl-H_4MPT^+) with p-H_2 (Fig. 2, Supplementary Methods and Supplementary Fig. 1). For a comparison, these experiments were also performed with normal hydrogen (n-H_2), which refers to H_2 with its nuclear spin states in room temperature thermal equilibrium. In the control experiment with n-H_2 (Fig. 2b), only the singlet of thermally polarized free dissolved H_2 was visible, whereas the triplet for free dissolved HD, which was expected according to Fig. 1c when working in deuterated buffer, is below the noise level. If p-H_2 was used instead (Fig. 2a), signal enhancement lifts the HD triplet above the noise and a signal with a mixed signal phase is observed for H_2.

The PHIP experiments can be repeatedly performed with the same sample (Supplementary Discussion, Supplementary Figs. 10–12 and Supplementary Tables 1 and 2). Signal enhancement for both H_2 and HD was sufficiently strong to be observed in a single scan at 1 µM jHmd concentration, which demonstrates the high sensitivity of PHIP.

Enhancement only occurs in the presence of jHmd and methenyl-H_4MPT^+ (Supplementary Fig. 9). Moreover, temperature and pD dependence of the PHIP effects coincide with the regions of high enzyme activity (Supplementary Figs. 14 and 15). The deuterium cation based pH is pD = $-\log_{10}$ a(D^+), with a(D^+) as the D^+ activity. The PHIP effects are quenched if His_{14} (Fig. 1a) is mutated to alanine (see H14A-jHmd mutant in Supplementary Fig. 13 and Supplementary Table 3). This confirms the link of PHIP creation to Hmd catalysis, for which His_{14} is essential.

Isotope labelling studies (^{2}H, ^{13}C and ^{57}Fe) support PHIP mechanisms involving only the two spins originating from p-H_2 (Supplementary Fig. 13 and Supplementary Table 3). The PHIP effects on H_2 and HD originate from two mechanisms that are both driven by coherent spin evolution. The minimum mechanistic model that is required to explain the hyperpolarization of H_2 and HD is given in Supplementary Fig. 22b and schematically summarized in Fig. 2c. For both the H_2-PHIP and the HD-PHIP, p-H_2 needs to add to the catalytic site to create an enzyme-bound state in which the two hydrogen atoms are inequivalent and still J-coupled.

The H_2-PHIP effect is created through reversible binding of H_2 into such an enzyme-bound state, resulting in a so-called partially negative line shape (PNL) effect[48]. From the phase of the signal, it can be concluded that the two protons originating from H_2 must have a positive mutual J_{HH}-coupling in the bound state producing the PNL[48]. While coordinated to the complex, parahydrogen converts into ortho-hydrogen. The NMR signal of the latter is then observed as a signal-enhanced PNL.

The HD-PHIP is also caused by spin evolution under strong J-coupling in a transiently formed enzyme-bound state, but in this case, hydrogen isotope exchange with the solvent is further required (Fig. 2c). The field dependence of the effect at low magnetic fields (Supplementary Discussion and Supplementary Figs. 8 and 23) is consistent with a strong J-coupling-mediated mechanism, referred to as oneH-PHIP[51] or NEPTUN[52–54], that dominates in the 1 mT to 7.1 T range (Supplementary Discussion). The match to the field profile expected for the J-coupling-mediated mechanism (Supplementary Discussion and Supplementary Fig. 23b, blue trace) is better than to the steeper profile expected for the alternative mechanism. The alternative mechanism could create polarization on HD through coherent evolution under residual dipolar couplings (RDCs)[55–57] under self-alignment (Supplementary Discussion, Supplementary Fig. 23b, orange trace and Supplementary Table 21), related to the SWAMP effect[58]. With increasing field, the RDC-driven mechanism should take over at some point, yet the data we collected (up to 21.1 T) can be well described considering only the J-coupling-mediated mechanism (Supplementary Discussion).

https://doi.org/10.1038/s41929-024-01262-w

As implied in Fig. 2c, observation of the HD-PHIP effect should be accompanied by the hyperpolarization of water. This effect becomes apparent at higher Hmd concentrations and temperatures (Fig. 3, Supplementary Fig. 10 and Supplementary Table 1), in particular when using an experiment with presaturation of the thermal water signal (Supplementary Fig. 2). Negative hyperpolarization is observed on HDO (Fig. 3), with the expected opposite sign to the HD-PHIP hyperpolarization. Heterolytic cleavage of p-H_2 by Hmd thus produces positive polarization on the hydride (H^-), which can react with D^+ to form HD, and negative polarization on the proton (H^+), which diffuses out of the enzyme into the bulk water. If it is the closed active site bearing methenyl-H_4MPT$^+$ (Fig. 1a) that produces this PHIP effect, the hyperpolarized H^- should also reduce the substrate according to Fig. 1b, leading to methylene-H_4MPT selectively hyperpolarized at the (C14a)$H_{pro\text{-}R}$ position. Indeed, the expected positive hyperpolarization can be observed at the ^{1}H chemical shift (δ_H) and with the $^1J_{CH}$ reported for the $(C_{14a})H_{pro\text{-}R}$ ($\delta(^1H_{C14a,pro\text{-}R})_{lit}$ = 4.9–5.05 ppm (refs. 32,39,59), $^1J(C_{14a},H_{pro\text{-}R})_{lit}$ = 158 Hz (ref. 59)) (Fig. 4). Transfer of hyperpolarization from the $(C_{14a})H_{pro\text{-}R}$ to the ^{13}C-labelled C_{14a} position further yields the corresponding hyperpolarized ^{13}C signal (Fig. 5 and Supplementary Fig. 16), close to the literature-reported ^{13}C chemical shift (δ_C) ($\delta(^{13}C_{14a})_{lit}$ = 69.87 ppm)[60]. This suggests that an intermediate along the Hmd catalytic cycle acts as the common source of hyperpolarization on HD, HDO and methylene-H_4MPT. Since all PHIP effects disappear in the absence of methenyl-H_4MPT$^+$ and methylene-H_4MPT, this intermediate must be formed by the intact enzyme–substrate complex allowing the catalytic reaction.

Analysis of field-dependent H_2-PHIP and HD-PHIP effects

For the H_2-PHIP and HD-PHIP effects, which can easily be observed in single scan experiments, measurements were performed at three different static magnetic fields (B_0), in an attempt to characterize the bound-state intermediate creating these effects. For analysis of this data, we aimed at matching the experimental NMR data in spin dynamics simulations (Supplementary Methods and Supplementary Discussion). Here, we restrained the kinetic parameters used for the simulations by the experimentally observed isotope exchange kinetics (Supplementary Discussion) and we compared them with ^{1}H NMR parameters computed for different structural models[29,35] (Supplementary Methods and Supplementary Discussion) to check for consistency with previously proposed mechanistic models.

Hydrogen isotope exchange kinetics (Supplementary Discussion, Supplementary Figs. 17–20 and Supplementary Table 4) were analysed using a model that assumes only one bound-state geometry (Fig. 2c and Supplementary Fig. 17). As compared with the model chosen by Leroux et al.[61], we explicitly chose a model in which the two hydrogen atoms are distinguishable in the bound state, since this is required for the occurrence of PHIP effects. For Hmd, multiple isotope exchange events can happen for one H_2 binding event (Fig. 1c)[33]. In our kinetics models, we implemented multiple isotope exchange events by assuming that isotope exchange ($H^+ \rightleftarrows D^+$) occurs at only one of the hydrogen positions in the bound state and that mutual exchange between the two hydrogen positions is possible, which enables us to estimate upper bounds for the rate of mutual exchange (k_{ex}). For simplicity, hydrogen isotope exchange kinetics were characterized at pD 6.0, where net kinetic isotope effects for this reaction are small[33]. During analysis, we therefore neglected kinetic isotope effects.

Structural models for Hmd were optimized at a combined quantum-mechanics/molecular-mechanics (QM/MM) level of theory, and ^{1}H chemical shifts (δ_H) and mutual ^{1}H–^{1}H J-couplings (J_{HH}) for

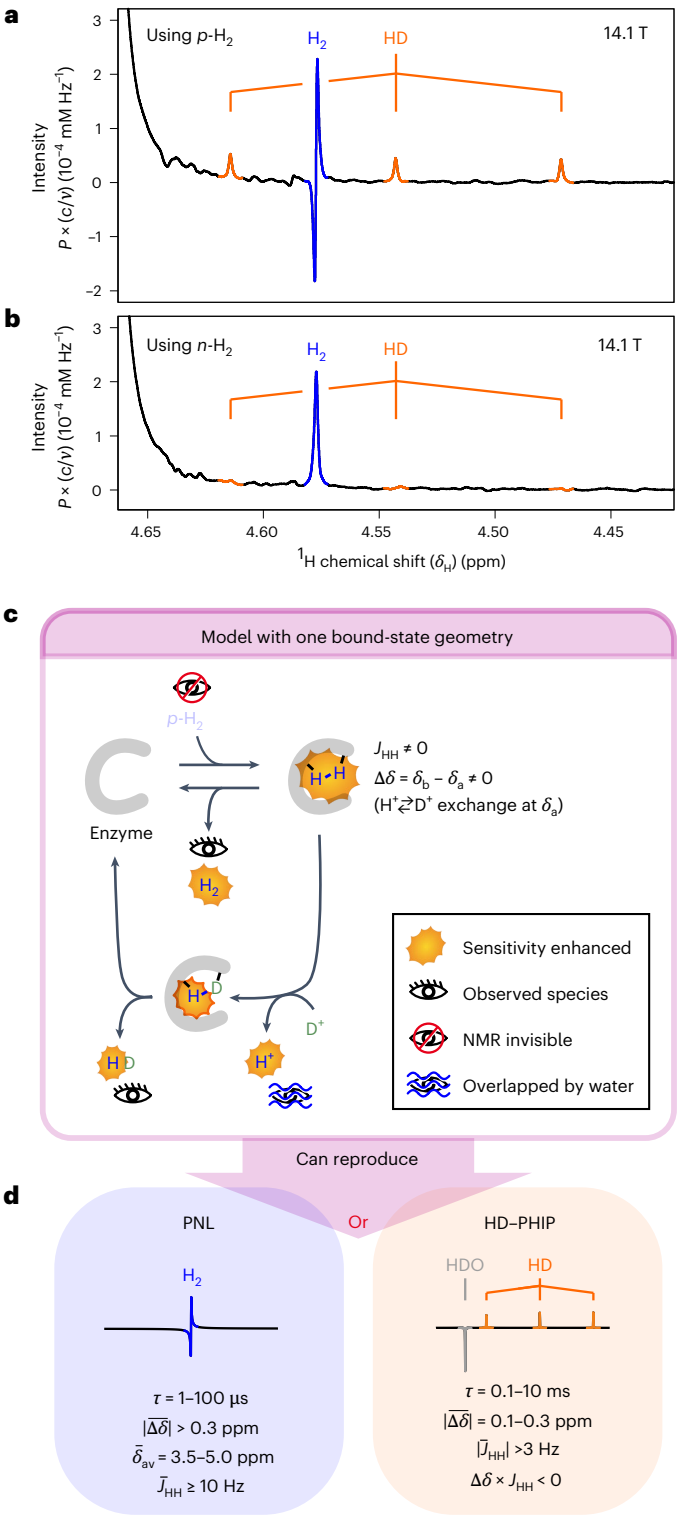

Fig. 2 | ^{1}H-PHIP effects observed on dissolved hydrogen in the presence of [Fe]-hydrogenase. a,**b**, Dihydrogen regions of the single-scan ^{1}H-NMR spectrum observed after supplying either p-H_2 (87% enrichment) (**a**) or n-H_2 (**b**) to a sample containing [Fe]-hydrogenase and substrate for 15 s at 309 K (pulse sequence; Supplementary Fig. 1). Compare with Supplementary Fig. 9. The sample was prepared from 1 µM jHmd and 3 µM [^{13}C]-CH_2=H_4MPT in D_2O buffer (pD 6.0, 1 mM EDTA and 120 mM potassium phosphate). Data are presented on a field-invariant absolute intensity scale (P, polarization; c, concentration; ν, frequency), as detailed in Supplementary Information. **c**, A pictographic scheme of the model with one bound-state geometry. The complete model is shown in detail in Supplementary Fig. 22b. **d**, A summary of the experimental constraints obtained from modelling the B_0-dependent data using the model with one bound-state geometry (PNL in Supplementary Discussion and Supplementary Figs. 26 and 27 and HD-PHIP, scenario B in Supplementary Discussion and Supplementary Fig. 28).

https://doi.org/10.1038/s41929-024-01262-w

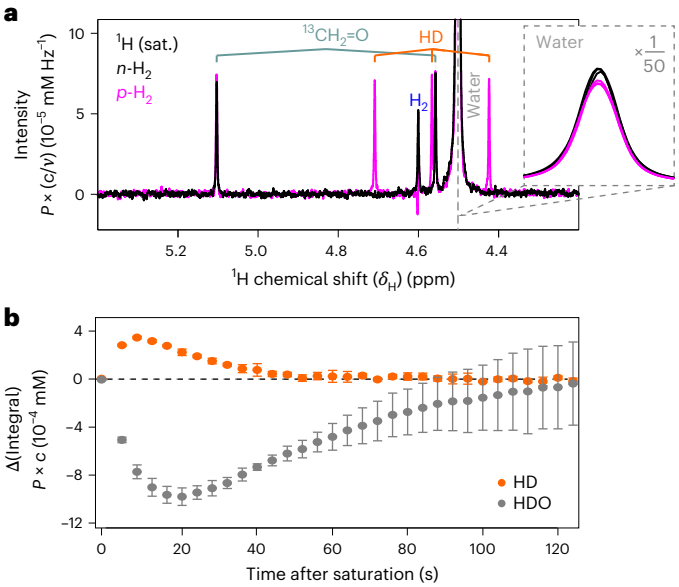

Fig. 3 | PHIP effects observed for water. a, An overlay of single-scan ^{1}H spectra acquired after supplying p-H$_2$ (magenta, 99% enrichment) or n-H$_2$ (black) to a sample containing 12 µM jHmd, 120 µM ^{13}CH$_2$=H$_4$MPT and 10 mM formaldehyde-^{13}C in D$_2$O buffer (pD 7.0, 1 mM EDTA and 120 mM potassium phosphate). Experiments were performed at 327 K and 7.1 T, using a ^{1}H-PHIP experiment with signal saturation (sat.) before acquisition (Supplementary Fig. 2). The insert shows the water signals overlaid that were obtained in three repetitions of the experiment with p-H$_2$ or with n-H$_2$. **b**, Time evolution of the HD (orange) and HDO signal integrals after stopping the signal saturation. The graph displays the difference between the integrals obtained in the p-H$_2$ and the n-H$_2$ experiments. The average and the s.d. over the three repetitions are shown.

the hydrogen atoms within the active site were computed (Supplementary Discussion, Supplementary Figs. 38–44 and Supplementary Tables 13–20). The QM/MM models were based on the crystal structure of the substrate-bound closed state of Hmd[29], as well as on the closed-state structural model by Finkelmann et al.[35], derived from the open-state crystal structure of a C176A mutant[31], by aligning the subunits using the crystal structure of the closed state apoenzyme[62]. For the catalytic cycle proposed in ref. 29, the results are summarized in Fig. 6 (see also Supplementary Table 14). We also investigated the scenario where H$_2$ activation proceeds via the thiol position rather than the oxypyridine pathway shown in Fig. 6, using the models by Finkelmann et al.[35] and models based on the most recent crystal structure (Supplementary Fig. 39 and Supplementary Table 16).

Spin dynamics simulations were performed under quasi-lossless conditions (slow relaxation and no competing reactions) (Supplementary Methods, Supplementary Discussion and Supplementary Table 9) providing the expected PHIP signal shapes for H$_2$ and HD, the effects from varying B_0 and an upper-bound limit for the intensity expected. During all analyses (Supplementary Discussion), we therefore only put restraints on the underestimation of PHIP intensities, not on the overestimation.

Modelling of the PHIP effects for H$_2$ (Supplementary Discussion, Supplementary Figs. 22a and 24–27 and Supplementary Tables 5–7) indicates that the average chemical shift of the two hydrogen atoms in the bound state is in the range of δ_{av} = 3.5–5.0 ppm, with the best fits obtained for δ_{av} = 4.3 ppm and with chemical shift differences around $\Delta\delta$ = 6–12 ppm (Supplementary Figs. 26 and 27). The time-averaged J_{HH}-coupling in the bound state should be $\bar{J}_{PNL} \geq 10$ Hz, with best fits obtained for couplings in the range of $\bar{J}_{PNL} = 50 - 300$ Hz(Supplementary Fig. 26 and Supplementary Table 7). The constraints obtained by analysing PNL and HD-PHIP in the model with one bound-state geometry (Fig. 2c and Supplementary Fig. 22a,b) are summarized in Fig. 2d.

To reproduce the PNL data in our simulations, a rapid exchange between an enzyme-bound ensemble in which the two atoms from p-H$_2$ are distinguishable and an ensemble in which they are indistinguishable by NMR (either dissolved H$_2$ or an enzyme-bound ensemble in which the two atoms are rapidly exchanging on the microsecond timescale) is required (Supplementary Discussion, Supplementary Fig. 26 and Supplementary Table 6). Herein, we use the term 'ensemble' for a group of reaction intermediates that interconvert rapidly enough to be indistinguishable on the NMR timescale (that is, microsecond to millisecond). The interconversion rates between these ensembles need to be much faster (~10^4-fold) than the apparent rate constants for association (k_a) and dissociation (k_d) for the net hydrogen isotope exchange reaction

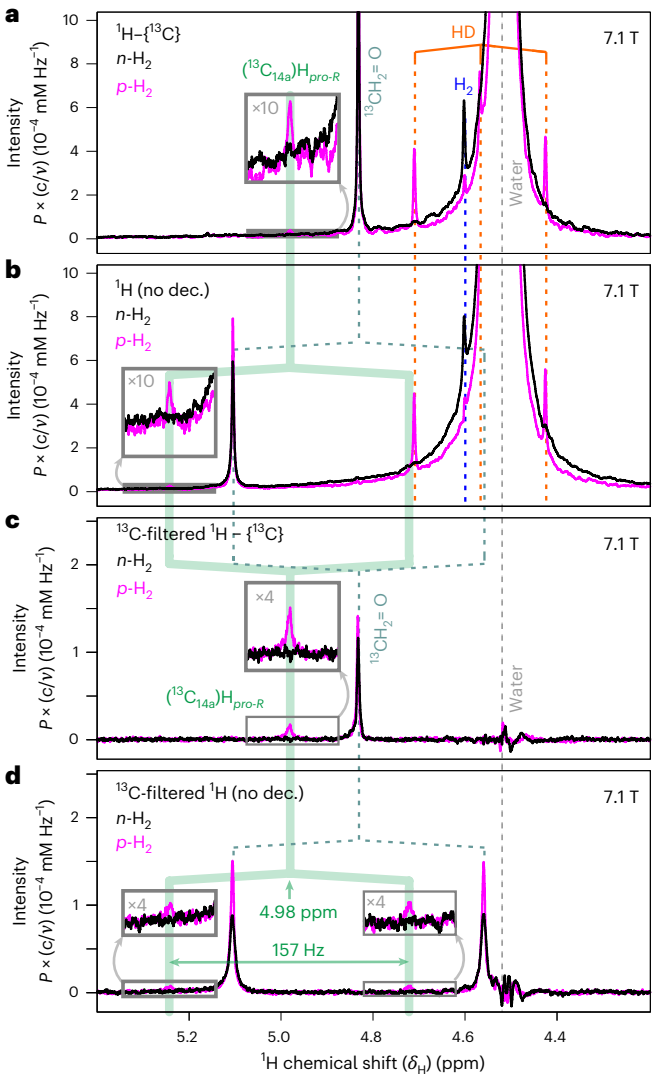

Fig. 4 | ^{1}H-PHIP effect observed for (C_{14a})$H_{pro\text{-}R}$. a–**d**, The ^{1}H spectra acquired for identification of the (C_{14a})$H_{pro\text{-}R}$ PHIP effect, using four different experiments: ^{1}H-experiments without ^{13}C filtration (**a** and **b**; sequence in Supplementary Fig. 1) and with ^{13}C filtration (**c** and **d**; sequence in Supplementary Fig. 3) were acquired with (**a** and **c**) or without (**b** and **d**) ^{13}C decoupling (dec.) during acquisition. Overlays of experiments using p-H$_2$ (magenta, 99% enrichment) or n-H$_2$ (black) are shown in all cases, and the signal region for (C_{14a})$H_{pro\text{-}R}$ in the free form of ^{13}CH$_2$=H$_4$MPT (not bound to Hmd) is highlighted by green traces and amplified in the inserts. In all cases, high concentration samples were used (sample conditions stated in Fig. 3 legend), experiments were performed at 327 K and signals were accumulated over 16 scans (four treatments with p-H$_2$ or n-H$_2$, with an accumulation of four scans after each treatment). Formaldehyde-^{13}C (^{13}CH$_2$=O) was added to improve sample stability. Different signal intensities for formaldehyde result from different degrees of formaldehyde deuteration due to the isotope exchange promoted by Hmd.

https://doi.org/10.1038/s41929-024-01262-w

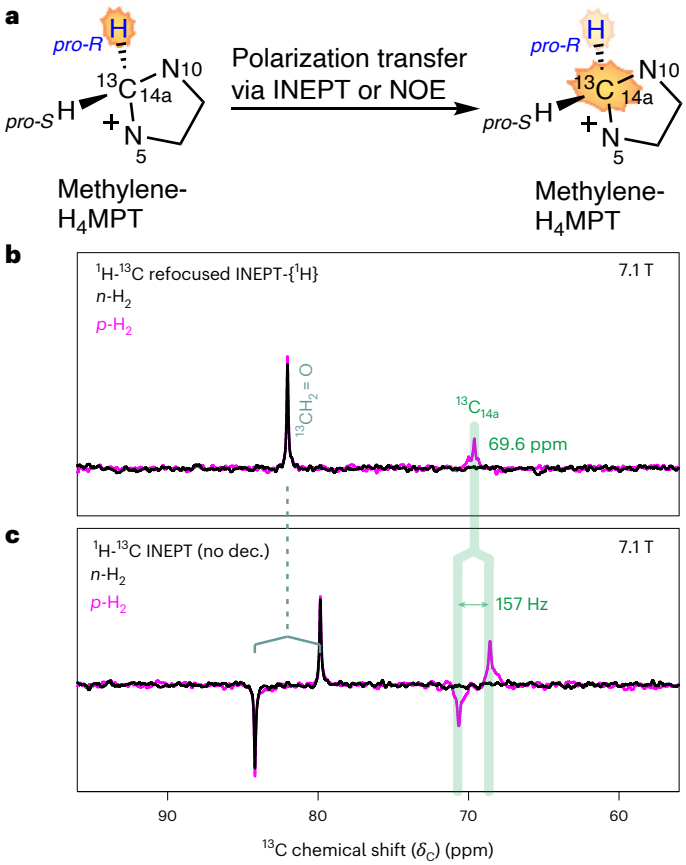

Fig. 5 | Transfer of hyperpolarization from $(C_{14a})H_{pro\text{-}R}$ to C_{14a}. **a**, Scheme of polarization transfer from $(C_{14a})H_{pro\text{-}R}$ to $^{13}C_{14a}$ using insensitive nuclei enhancement by polarization transfer (INEPT) (Supplementary Fig. 4). **b**, Refocused INEPT experiment with ^1H decoupling during acquisition. **c**, INEPT experiment without refocusing and decoupling. Overlays of experiments using *p*-H_2 (magenta, 99% enrichment) or *n*-H_2 (black) are shown. Data collected using Nuclear Overhauser Effect (NOE)-driven hyperpolarization transfer to $^{13}C_{14a}$ (Supplementary Fig. 5) are shown in Supplementary Fig. 16. High-concentration samples were used (sample conditions as stated in Fig. 3 caption, and for **a** and **b** only, 2 mM formaldehyde-^{13}C was used), experiments were performed at 327 K and signals were accumulated over 512 scans (512 treatments with *p*-H_2 or *n*-H_2).

(Supplementary Table 4 and Supplementary Figs. 25 and 26), resulting in a lifetime for the enzyme-bound ensemble with distinguishable hydrogen positions in the range of $\tau_{PNL} \approx 1$ µs to 100 µs.

The most reasonable structural explanation for the enzyme-bound ensemble with distinguishable hydrogen positions causing the PNL are iron hydrides such as structure **4** (Fig. 6, Supplementary Table 14, model A2, and see also models C/G3 and C/G4 in Supplementary Fig. 39 and Supplementary Table 16). The scenario that H_2 is activated by the oxypyridine rather than the S_{Cys176} is hereby clearly favoured due to the larger J_{HH}-couplings and the better fit to the required chemical shift range in the computed structures. Moderate agreement between the experimentally observed and the simulated spectra is obtained for example for model A2, corresponding to structure **4**, when assuming intermediate lifetimes around 16 µs (Supplementary Table 5).

For model A1 (Supplementary Table 14), corresponding to structure **3** in Fig. 6, the best-fit ranges for the PNL perfectly match the NMR parameters computed. Consequently, a perfect fit of simulated and measured spectra can be obtained for this model (Supplementary Table 5). Despite this finding, it appears unlikely that Fe-η^2-H_2 species such as structure **3** are causing the PNL, since fast mutual exchange of the hydrogen atoms in dihydrogen ligands[63–65] should suppress the evolution of PHIP effects within these ligands. Interaction of the dihydrogen ligand with the oxypyridine base in structure **3** (Supplementary Table 14, A1) considerably raises the barrier of rotation as compared with the case where the base is protonated (Supplementary Table 16, C1, and compare Supplementary Figs. 41 and 42), yet it still appears unlikely that the rotation is sufficiently hindered that PHIP effects can evolve in structure **3**. Electronic structure simulations suggest that the rate for mutual site exchange for the η^2-H_2 ligand (k_{ex}) is reduced from the single-digit THz range for C1 to around 1 GHz for A1 (Supplementary Discussion and Supplementary Figs. 41 and 42). To produce the observed PHIP signals, however, k_{ex} must not exceed 100 kHz (Supplementary Table 6).

Thus, iron hydrides such as structure **4** (Fig. 6) are the most likely candidates for causing the PNL effect observed. Our data suggest that formation of the iron hydride involved is not rate limiting for substrate reduction, in line with earlier studies of kinetic isotope effects, which indicated that a reaction step other than H_2 activation is rate-limiting for $CH{\equiv}H_4MPT^+$ reduction by Hmd[66].

The HD-PHIP is created in a transiently formed intermediate with a lifetime of $\tau_{HD\text{-}PHIP} \approx 100$ µs–10 ms (Supplementary Discussion, Supplementary Figs. 28 and 29 and Supplementary Table 8). In general, a J_{HH}-coupling of small amplitude ($|J| > 3$ Hz) and small chemical shift differences ($0.1 \text{ ppm} \leq |\Delta\delta| \leq 1$ ppm) are sufficient to create the observed effects (Fig. 2d). Spectra can be reproduced in simulations using the kinetic parameters extracted from the net isotope exchange (Supplementary Discussion and Supplementary Fig. 28), suggesting that the intermediate creating the HD-PHIP is the one accumulating right before the isotope exchange step. For mechanisms with J_{HH} evolution and isotope exchange happening in the same bound state (for example, Fig. 2c and Supplementary Figs. 21 and 22b), simple rules relate the sign of the HD-PHIP signal to the signs of $\Delta\delta$ and J_{HH} (Supplementary Discussion), which favour the scenario where $J_{HH} < 0$.

Among the computed structural models, structure **5** is compatible with a $J_{HH} < 0$ according to our *J*-coupling computations (0 ± 3 Hz; SI 2.15). Another reasonable explanation may be that the hydride in structure **4** recombines with a D^+ to form an Fe-η^2-HD species, in which the H^+ from *p*-H_2 is still bound to the pyridinol position. Structural modelling suggests that the time-averaged J_{HH}-coupling within such a complex could be slightly negative (-1 ± 3 Hz, see structure C1 in Supplementary Table 16, Supplementary Fig. 41 and Supplementary Discussion). With the differences in kinetics and the preference for different signs for J_{HH}, the separate modelling of PNL and HD-PHIP provides clear evidence that more than one bound-state ensemble is contributing to the two PHIP effects. This is underlined by the fact that different parameter sets need to be used for the model with one bound-state geometry (Fig. 2c and Supplementary Fig. 22b) to reproduce the PNL or the HD-PHIP (Fig. 2d). Considering the facile reversibility of the catalytic reactions and the flat free energy profiles predicted for Hmd[20,29,34] (Supplementary Figs. 43 and 44), it is unsurprising to find that multiple bound-state intermediates must be populated substantially.

When two bound-state ensembles are included, HD-PHIP and H_2-PHIP signals (Fig. 7b) and isotope exchange kinetics (Fig. 7c) can be simultaneously reproduced. A schematic representation of the model with two bound-state geometries is given in Fig. 7a and the full model is shown in Supplementary Fig. 22c (compare with Fig. 2c and Supplementary Fig. 22b). Due to the very different kinetics, the *J*-coupling causing the PNL must be present in a different ensemble than the $H^+ \rightleftarrows D^+$ exchange (Supplementary Discussion and Supplementary Fig. 25). To reproduce both, we place the *J*-coupled intermediate causing the PNL in the early bound-state ensemble (ensemble 1), separated from the isotope exchange reaction in the later bound-state ensemble (ensemble 2). Different modelling scenarios for the HD-PHIP are compatible with the data (Fig. 7, Supplementary Discussion, Supplementary Tables 9–11 and Supplementary Figs. 30–32), indicating that it could be the same or two different *J*-coupled intermediates causing the PNL and the HD-PHIP. The model outlined reproduces key features

https://doi.org/10.1038/s41929-024-01262-w

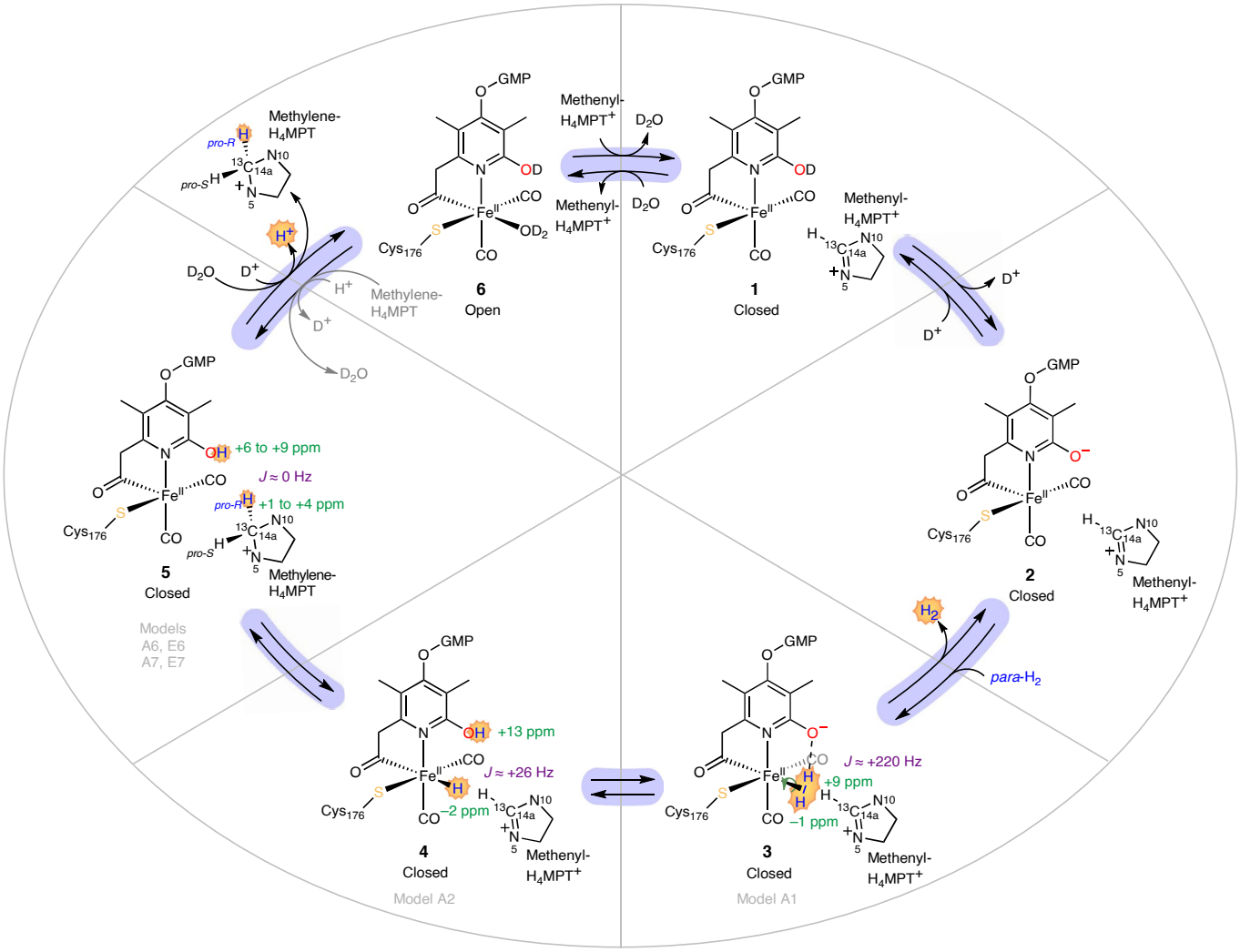

Fig. 6 | Refined Hmd catalytic cycle. The suggested catalytic cycle, adjusted for use with *p*-H_2 in D_2O buffer. The NMR parameters obtained from structural modelling are indicated. Green, chemical shift ranges from different models (ppm); purple, typical *J*-coupling (Hz); grey, model numbers (Supplementary Tables 14 and 16). GMP, guanosine monophosphate. For methenyl-H_4MPT^+ and methylene-H_4MPT, only the imidazolium and imidazolidine rings are depicted. The reaction from **6** to **5** is greyed out, since the back-reaction in the hyperpolarized nuclear spin state appears unlikely.

expected from the mechanism shown in Fig. 6, such as the creation of a short-lived intermediate compatible to an iron hydride (structure **4**) upon hydrogen activation, which further reacts to an intermediate (structure **5**) that is expected to be longer lived (Supplementary Fig. 43) and which can perform hydrogen isotope exchange to form hyperpolarized HD and HDO.

Characterization of bound states by saturation transfer

The PHIP effects described thus far are observed on product species that are released from the catalytic cycle and detected in solution. From these signals, information about the hydrogen-bound states can be obtained because the PHIP effects are created while the hydrogen atoms are bound to the active site. Products with slow ^{1}H relaxation provide the highest sensitivity due to a narrow linewidth for detection and because the hyperpolarized species can be effectively accumulated in solution.

Direct detection of the bound intermediate states themselves should generally be possible. This is, however, more challenging because of the small enzyme concentration and because the bound-state signals are expected to be much broader. Fortunately, PHIP experiments provide an elegant way of observing bound intermediates with outstanding sensitivity.

PHIP experiments can be combined with the chemical exchange saturation transfer (CEST) approach[67–69], a method we refer to as PHIP-CEST[48]. CEST indirectly detects transiently formed species of low concentration through their chemical exchange with an abundant species[68,69]. In our case, saturation is transferred from the bound-state intermediates onto the easily detectable reaction products. The inherently high detection sensitivity of the CEST experiment is further boosted through hyperpolarization[48,70,71].

Using PHIP-CEST[48] for the Hmd system (Supplementary Figs. 6 and 7), we observed CEST effects in the form of altered signal intensities for H_2 and HD signals, and altered shape of the H_2 signal, as a function of the CEST irradiation frequency (Fig. 8 and Supplementary Figs. 33–35). The H_2 signal shape changes from the PNL shape to an in-phase signal undergoing a switch of sign and then back to the PNL (Fig. 8b, inserts). The CEST effects saturate at spin-lock fields between 0.5 and 1 kHz (Supplementary Figs. 34 and 35), thus providing an estimate for the lifetime of the intermediates of $\tau_{PHIP\text{-}CEST} \approx 1$–2 ms.

Two CEST effects are observed at similar positions for detection on the H_2 and the HD-PHIP signals. The CEST effect at 10.5 ppm (±0.5 ppm) is particularly well resolved in the HD-PHIP-CEST experiment (Fig. 8a), falling into the chemical shift range of acidic protons. The position of the second effect can only roughly be estimated (around 3 ± 3 ppm)

https://doi.org/10.1038/s41929-024-01262-w

due to its proximity to the on-resonance saturation for free hydrogen (at 4.6 ppm). Notably, no PHIP-CEST effects were observed in the $\delta_H < -10$ ppm region, which is characteristic for metal hydrides. This is well in line with the computed chemical shifts for hydride species (Fig. 8 and Supplementary Tables 14 and 16), for which in all cases, $\delta_H > -7$ ppm.

The PHIP-CEST curves can be reproduced qualitatively in simulations, assuming a single bound-state ensemble with chemical shifts of 10.5 ppm (±0.5 ppm) and 4 ppm (±2 ppm) and with hydrogen isotope exchange with D_2O happening at 10.5 ppm (Supplementary Discussion and Supplementary Table 12), using kinetic parameters that reproduce the measured hydrogen isotope exchange (Supplementary Table 12 and Supplementary Fig. 36). The 10.5 ppm fall into the chemical shift range estimated for the pyridinol position of FeGP, as well as for previously suggested thiol-ligand intermediates (H–S–Cys176) (see ranges indicated in grey in Fig. 8a; see also Supplementary Discussion, Supplementary Tables 14 and 16)[30,34]. Considering the 100-fold reduction in $H^+ \rightleftarrows D^+$ exchange activity in the H14A-jHmd mutant[30] (Supplementary Table 3), the assignment to the pyridinol position appears reasonable. For the 4 ppm position, the $(C_{14a})H_{pro\text{-}R}$ position of $CH_2{=}H_4MPT$ in structure **5** falls into the expected range, which agrees with the model shown in Fig. 6.

To reproduce the PHIP-CEST data, a negative mutual J_{HH}-coupling between the two atoms originating from *p*-H_2 needs to be assumed (Supplementary Fig. 37). An intermediate with $J_{HH} < 0$ thus clearly has to participate in the Hmd catalytic mechanism, and it appears likely that this PHIP-CEST and the HD-PHIP are probing the same intermediate. The lifetime estimate from PHIP-CEST ($\tau_{PHIP\text{-}CEST} \approx 1$–$2$ ms) matches the best-fit estimate for the bound-state lifetime from isotope exchange notably well ($\tau_{isotope\ exchange} = (k_d + k_{HD} + k_{ex})^{-1} \approx 1.7$ ms), suggesting that the intermediate probed is the intermediate accumulating before the isotope exchange step.

Considering the good match of the computed chemical shifts with the positions of the PHIP-CEST effects, the compatibility of the computed couplings with a negative J_{HH}-coupling between the pyridinol position and the $(C_{14a})H_{pro\text{-}R}$ position of $CH_2{=}H_4MPT$ and considering the computed reaction trajectory (Supplementary Fig. 43), the intermediate probed by PHIP-CEST is most probably structure **5** of Fig. 6.

Conclusions

Here, we demonstrate that sensitivity-enhanced NMR can be used to study bound hydrogen intermediates in hydrogenase catalysis. The NMR technique first applied here to study a diamagnetic metalloenzyme is particularly suitable for investigating transient hydrogen intermediates during catalysis because it selectively enhances the signals of bound hydrogen species. Studying these bound hydrogen species, particularly in diamagnetic intermediates, remains a challenge for established techniques. Our approach therefore bridges a substantial gap in biophysical characterization abilities.

The PHIP effects on H_2, HD, HDO and at the $(C_{14a})H_{pro\text{-}R}$ position of methylene-H_4MPT are only observed if the active enzyme–substrate complex forming the active site is used. Thus, these PHIP effects emerge from the active catalytic cycle of Hmd. Highly sensitive PHIP-CEST experiments enabled us to directly observe the hydrogen atoms stemming from *p*-H_2 in an active-site bound state under turnover conditions. Comparison of the experimental data with NMR spectrum simulations, using parameters from measured kinetics and QM/MM structural modelling, enabled us to characterize two intermediates along the Hmd catalytic cycle, which had previously not been characterized experimentally. The two intermediates fit the iron hydride (structure **4**) and the enzyme-bound reduced substrate

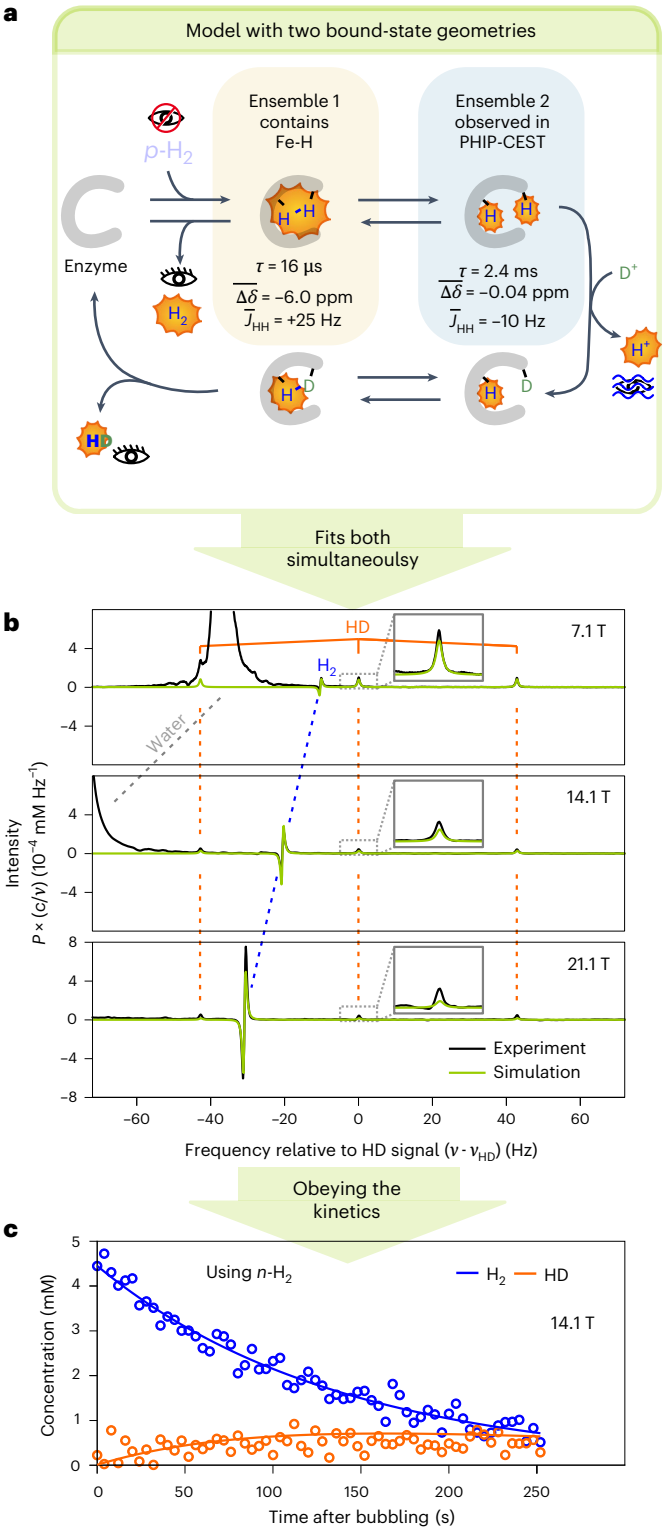

Fig. 7 | Joint modelling of PNL, HD-PHIP and isotope exchange kinetics. **a**, A pictographic scheme of the model with two distinct bound-state geometries. Compare with the model with one bound-state geometry in Fig. 2c. **b**, An overlay of measured (black, single scan) and simulated (green) ^{1}H-PHIP spectra for three B_0 fields. Simulations used the model with two bound-state geometries (**a**, Supplementary Fig. 22c, Supplementary Discussion and Supplementary Tables 9 and 10). Selected parameters for the simulations in **b** are indicated in the figure. H_2 and water peaks remain at the same chemical shifts (ppm) at all three B_0 fields; however, a hertz scale, relative to the HD frequency, was chosen here for clearer visualization. Sample conditions are as stated for Fig. 2a. Supplementary Fig. 12 and Supplementary Table 2, compare spectra for multiple samples. **c**, The measured and simulated isotope-exchange kinetics for data shown in **b**. The spectrum collected immediately after treating the sample with *n*-H_2 gas is shown in Fig. 2b.

https://doi.org/10.1038/s41929-024-01262-w

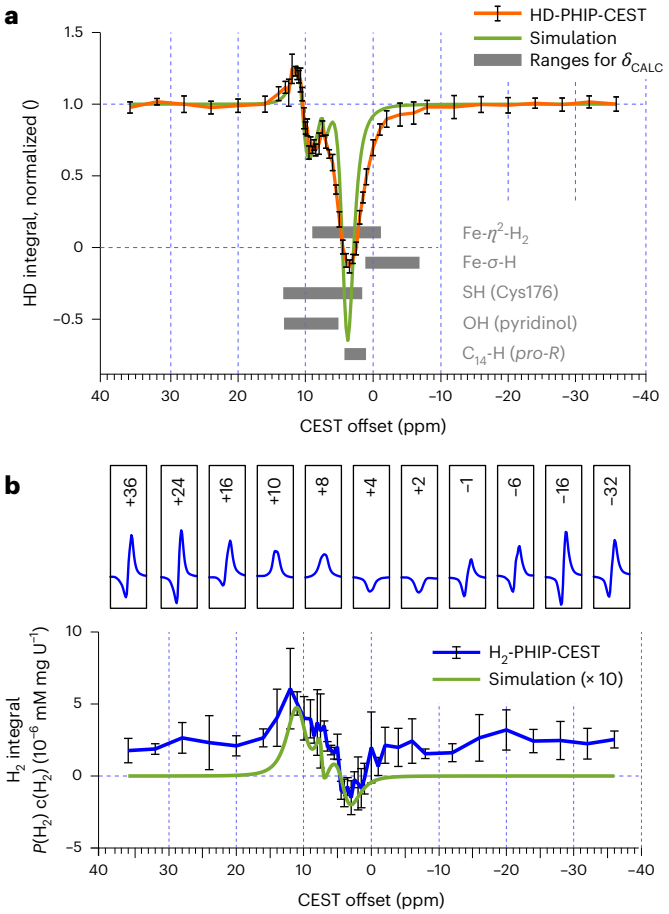

Fig. 8 | Hyperpolarized CEST experiments for the identification of reaction intermediates. PHIP-CEST experiments performed at 309 K and 14.1 T (600 MHz), with sample conditions as for Fig. 2. **a**, The HD-PHIP-CEST profile obtained from multiple quantum-filtered experiments (Supplementary Fig. 7), using an 8 s saturation with $\gamma B_1 = 666$ Hz (γ, gyromagnetic ratio). The HD signal integral, normalized to the off-resonance integral, measured at −36 ppm, is shown in orange. Data from five samples were averaged, collecting one single-scan spectrum per offset and per sample. The error bars indicate s.d. A simulated HD-PHIP-CEST profile (Supplementary Discussion and Supplementary Table 12) is overlaid. In grey, the ranges of computed chemical shifts (δ_{CALC}) for hydrogen species obtained from multiple different QM/MM models (Supplementary Discussion and Supplementary Tables 13–16) are indicated. **b**, The H_2-PHIP-CEST experiment according to Supplementary Fig. 6, using a 2 s saturation with $\gamma B_1 = 1{,}333$ Hz. The H_2 lineshape observed after irradiating at different offsets and the corresponding H_2 line integral (polarization × concentration), normalized by sample activity for hydrogen isotope exchange (activity range of 68–41 U mg^{-1}). The average from three samples is shown with s.d. as error bars. A simulated profile obtained using the same simulation parameters as in **a** is shown in green. Simulated data are upscaled tenfold for better visualization of the qualitative agreement obtained.

(structure **5**), with hydrogen activation proceeding with the oxypyridine as the active base, supporting the previously proposed mechanism[29] (Fig. 6).

The techniques used here can now be used as a general approach for unravelling the catalytic mechanisms of hydrogenases and their model catalysts. In addition, given the high sensitivity of this technology, it holds promise regarding its application to microbial cells, and with regard to exploring hydrogen metabolism in vivo. Ultimately, we have established an approach for studying the catalytic mechanisms of hydrogen activating enzymes, which could help tailoring hydrogen converting (bio)catalysts towards higher productivity in hydrogen production or conversion.

Methods

Cultivation of *M. marburgensis*

Methanothermobacter marburgensis was cultivated anaerobically in a 10 l fermenter under continuous flow of a gas mixture composed of $H_2/CO_2/H_2S$ (80%/20%/0.1%)[72]. The medium consisted of 40 mM NH_4Cl, 50 mM KH_2PO_4, 24 mM Na_2CO_3, 0.5 mM nitrilotriacetic acid, 0.2 mM $MgCl_2\,6\,H_2O$, 1 µM $CoCl_2\,6\,H_2O$, 1 µM $Na_2MoO_4\,2\,H_2O$, 50 µM $FeCl_2$, 5 µM $NiCl_2$ and 20 µM resazurin (final concentrations)[72]. To isolate H_4MPT from the cells, *M. marburgensis* was cultivated in the full medium. In the case of Hmd purification, *M. marburgensis* was cultivated under nickel-limiting conditions, where $NiCl_2$ was omitted from the medium. In the nickel-limiting culture, a trace amount of nickel is supplied by erosion from the metal parts of the fermenter. For the preparation of ^{57}Fe-enriched FeGP cofactor, 50 µM [^{57}Fe]-$FeCl_2$ was added to the medium instead of non-enriched $FeCl_2$. [^{57}Fe]-$FeCl_2$ was prepared by the treatment of ^{57}Fe-enriched metal (96% enrichment) in 38% HCl solution. In the nickel-sufficient culture, when the culture reached an optical density (OD) of ~6–7 at the late exponential growth phase, the cells were collected. In the case of nickel-limiting condition, the culture growth, which started from 5% inoculation of pre-culture, became slower after overnight culture at OD ~4. The slow growth of the culture with doubling time of ~11 h under the nickel-limiting conditions continued until OD ~5–6. The culture in the fermenter was cooled down by circulating ice water and then anaerobically collected via continuous-flow centrifugation and the cells were stored at −75 °C. Chemicals were purchased from Sigma-Aldrich or Carl Roth.

Purification of Hmd from *M. marburgensis*

Purification of Hmd from *M. marburgensis* (mHmd) was performed under strictly anaerobic conditions in an anaerobic glove box (Coy Laboratories). Centrifugation was performed using a plastic tube with a screw cap and a rubber O-ring. Around 100 g of *M. marburgensis* cells were suspended in 200 ml of 50 mM potassium phosphate buffer pH 7.0 and sonicated (80% power of 100 W for six times of 8 min on/7 min off cycles) with a SONOPULS HD 200 from Bandelin using a VS 70T tip. The crude extract was centrifuged for 30 min at 140,000*g* and 4 °C. Ammonium sulfate powder was added to the supernatant until 60% saturation. After 20 min incubation on ice, the supernatant was centrifuged for 20 min at 13,000*g* and 4 °C, and then ammonium sulfate powder was added to the supernatant until 90% saturation. After another 20 min incubation on ice, the suspension was centrifuged for 20 min at 13,000*g* and 4 °C. Afterwards, the pellet was suspended in 15 ml of 50 mM 3-(*N*-morpholino)propanesulfonic acid (MOPS)/KOH pH 7.0. The suspension was dialysed at 4 °C overnight against 50 mM citrate/NaOH pH 5.0. The dialysed solution was centrifuged for 20 min at 17,000*g* and 4 °C, and the supernatant was applied to a Source 30Q column (300 ml column volume) equilibrated with 50 mM citrate/NaOH pH 5.0. The column was washed with 50 mM citrate/NaOH pH 5.0 containing 200 mM NaCl. Elution took place with a linear gradient from 200 mM to 500 mM NaCl in 500 ml. Fractions of 10 ml were immediately neutralized with 1.0 ml of 1 M MOPS/KOH pH 7.0 and 0.06 ml 1 M NaOH. Fractions containing mHmd were pooled and concentrated via an Amicon ultrafilter (30 kDa cut-off). Afterwards, the concentrated solution was applied to a HiPrep 26/10 desalting column equilibrated with H_2O. The elution was carried out with H_2O and the fractions containing mHmd were pooled and concentrated with an Amicon ultrafilter (30 kDa cut-off). Finally, purified mHmd was flash frozen in liquid nitrogen and stored at −75 °C. Chemicals were purchased from Sigma-Aldrich or Carl Roth. The enzyme activity assays are described in Supplementary Methods.

Extraction of the FeGP cofactor

The FeGP cofactor was extracted from 100 mg of mHmd by incubation in 60% MeOH, 1 mM 2-mercaptoethanol and 1% NH_3 in a final volume of 12 ml for 15 min at 40 °C. Subsequently, the FeGP cofactor

was separated from the denatured protein through filtration with an Amicon filter (10 kDa cut-off). The filtrate was collected and evaporated at 4 °C. The concentrated FeGP cofactor solution (~50 µl) was diluted to 1 ml with 10 mM ammonium carbonate pH 9 containing 1 mM 2-mercaptoethanol. The five aliquots of 200 µl were stored in liquid nitrogen. Chemicals were purchased from Sigma-Aldrich or Carl Roth.

Production of jHmd apoenzyme

The apoenzymes of Hmd from *M. jannaschii* (jHmd), the wild type and the H14A mutant were produced in *E. coli* BL21(DE3)[38]. For a pre-culture, 100 ml Luria-Bertani medium with 30 µg ml^{-1} kanamycin were inoculated with a frozen glycerol stock of the *E. coli* cells harbouring the corresponding plasmid. The pre-culture was shaken at 37 °C overnight and used to inoculate 2 l of tryptone-phosphate (TP) medium[73], which contained 30 µg ml^{-1} kanamycin. When the culture reached an OD_{600} of 1, the expression of *jHmd* was induced with a final concentration of 1 mM isopropyl β-D-1-thiogalactopyranoside. After 3 h of expression, the cells were collected by centrifugation for 20 min at 13,000*g* and 4 °C. The cells were suspended in 50 mM MOPS/KOH pH 7.0 containing 1 mM dithiothreitol (DTT) and disrupted by sonication (80% power of 100 W with five times of 4 min on/4 min off cycles) using an MS 72 tip. The debris was removed via ultracentrifugation for 40 min at 130,000*g* and 4 °C, and the supernatant was heated for 15 min at 70 °C to denature the *E. coli* proteins. By centrifugation for 20 min at 13,000*g* and 4 °C, the denatured proteins were removed. Afterwards, ammonium sulfate powder was slowly added to a final concentration of 2 M. Then, the precipitated proteins were removed again via centrifugation for 20 min at 13,000*g* and 4 °C. The supernatant was applied to a Phenyl-Sepharose column (50 ml column volume) equilibrated with 50 mM MOPS/KOH pH 7 containing 1 mM DTT and 2 M ammonium sulfate. The proteins were eluted with a 200 ml linear gradient from 2 M to 0 M ammonium sulfate. Each 10 ml was fractionated and analysed by sodium dodecyl sulfate–polyacrylamide gel electrophoresis. The fractions containing jHmd were pooled and concentrated to 10 ml with an Amicon ultrafilter (30 kDa cut-off). Then, the solution was desalted by a HiPrep 26/10 desalting column equilibrated with 50 mM MOPS/KOH pH 7.0 containing 1 mM DTT. The apoenzyme was flash frozen and then stored at −75 °C. Chemicals were purchased from Sigma-Aldrich or Carl Roth.

Reconstitution of the jHmd holoenzyme

To reconstitute the jHmd holoenzyme, 125 µM of the apoenzyme (either wild type or H14A mutant) were mixed with 175 µM of the purified FeGP cofactor. To get rid of the non-incorporated FeGP cofactor, the solution was applied to a HiPrep 26/10 desalting column equilibrated with 10 mM MOPS/KOH pH 7.0. All procedures were performed under yellow light in an anaerobic tent. Chemicals were purchased from Sigma-Aldrich or Carl Roth.

Purification of H_4MPT and conversion to CH_2=H_4MPT, $^{13}CH_2$=H_4MPT and CD_2=H_4MPT

For the purification of H_4MPT, 130 g of *M. marburgensis* cells (nickel-sufficient growth condition) were suspended in 130 ml of 50 mM MOPS/NaOH pH 6.8 and heated to 60 °C in a water bath. *N*,*N*,*N*-trimethylhexadecan-1-aminium bromide was added to a final concentration of 1%, and the suspension was incubated for 6 min at 60 °C. Afterwards, the suspension was cooled down in an ice bath for 30 min. In an anaerobic chamber, the pH was adjusted to 3 using 100% formic acid and the suspension was centrifuged for 60 min at 6,800*g* and 4 °C. The supernatant was separated from the pellet and put on a Serdolit PAD II column (Serva) equilibrated with XAD buffer (H_2O-formic acid buffer (69:1), pH 3 adjusted by NaOH). The column was washed with XAD buffer and eluted with 15% methanol in XAD buffer. The H_4MPT-containing fractions were pooled and evaporated. Subsequently, the lyophilized preparation was solubilized in 50 ml of H_2O and pH was adjusted with 100% formic acid to 3. The solution was loaded on a Serdolit PAD I column (Serva) equilibrated with XAD buffer. The column was washed with 0.1% formic acid in H_2O and eluted with 30% methanol containing 0.1% formic acid in H_2O. The H_4MPT-containing fractions were pooled, lyophilized and the concentration was adjusted by adding H_2O. For the conversion of H_4MPT to CH_2=H_4MPT, $^{13}CH_2$=H_4MPT and CD_2=H_4MPT, 500 µl of 2 mM H_4MPT was mixed with 15 µl 200 mM HCHO, [^{13}C]-HCHO or [$^2H_2$]-HCHO. The conversion to CD_2=H_4MPT took place in D_2O. The converted solutions were evaporated and the concentrations were adjusted with H_2O or D_2O. [^{13}C]-HCHO or [$^2H_2$]-HCHO and D_2O were purchased from Cambridge Isotope Laboratories.

NMR sample preparation

NMR samples were prepared by mixing stocks of the corresponding forms of Hmd and methylene-H_4MPT with D_2O-buffer inside 5 mm NMR tubes under a stream of N_2 or Argon. All stocks were handled in brown-glass vials under inert atmosphere, using microlitre syringes. All sample handling was performed in the dark. Used sample concentrations are stated in the figure and table captions. After mounting the samples to the systems for bubbling NMR samples inside the NMR spectrometers, all samples were bubbled with N_2 for at least 1 min to convert the methylene-H_4MPT used for sample preparation to methenyl-H_4MPT^+ in situ.

Deuterated 120 mM potassium phosphate buffers containing 1 mM EDTA were prepared at varying pD (see figure captions) and degassed before use by bubbling with N_2.

D_2O (99.9%), K_3PO_4, 3-(trimethylsilyl)-1-propansulfonic acid and EDTA-dianhydride were purchased from Sigma-Aldrich. KD_2PO_4 was either also purchased from Sigma-Aldrich or prepared from KH_2PO_4 (Carl Roth) using isotope exchange with D_2O.

NMR instrumentation

NMR experiments were performed on four different liquid state spectrometers operating at 600 MHz (14.10 T, 5 mm cryoprobe), 900 MHz (21.15 T, 5 mm cryoprobe) or 300 MHz (7.05 T, 5 mm room temperature probes) ^{1}H resonance frequency. For instrument specifications and detailed instrument settings, see Supplementary Methods. Spectrometers were equipped with home-built bubbling set-ups for handling the samples under inert atmosphere and for saturating the solutions with different gases by gas bubbling while the sample resides inside the spectrometer. The bubbling set-ups were equipped with three gas channels (N_2, *p*-H_2 and *n*-H_2 or mixtures of N_2 and *n*-H_2) with flow control by needle valves and magnet valves switched during the NMR pulse sequence using the spectrometer's transistor-transistor-logic outputs. Gas pressure inside the sample volume was cycled between room pressure and 7 bar (gauge pressure), using pressure regulators at the inlets and a backpressure regulator at the gas outlet. Mixtures of N_2 and *n*-H_2 were prepared by pre-mixing at defined ratios in a storage container. *p*-H_2 was produced from *n*-H_2 by two different parahydrogen generators (Supplementary Methods). Measured *p*-H_2 enrichments are provided with all figures showing PHIP data. Chemical shifts were referenced against 3-(trimethylsilyl)-1-propansulfonic acid and concentrations were referenced using EDTA as internal standard, as described in Supplementary Methods.

NMR experiments

NMR experiments were performed according to the experiment schemes in Supplementary Figs. 1–8. Towards the start of all experiments, the samples were bubbled with N_2 for 30 s and subsequently with *p*-H_2, *n*-H_2 or mixtures of *n*-H_2 and N_2 for bubbling periods of $\tau_{bubbling}$ of 8 s (7 T instruments) or 15 s (14 T and 21 T instruments), with intermittent pressure release to atmospheric pressure. Sample pressure was maintained constant at 7.0 bar during acquisition. Detailed description of NMR measurement parameters is provided in Supplementary Methods.

NMR data representation

NMR data in this study are represented on field-independent absolute scales. We use $c \times P$ for integrals and $c \times P \times \nu^{-1}$ for intensities (where c is the analyte concentration and P is the nuclear spin polarization and ν is the frequency in Hz). For more details, see Supplementary Methods.

Characterization of hydrogen isotope exchange kinetics

Hydrogen isotope exchange kinetics ($H^+ \rightleftarrows D^+$ exchange) was characterized by bubbling neat n-H_2 or mixtures of n-H_2 and N_2 through samples with deuterated buffers (>96% ^2H) containing Hmd and methylene-H_4MPT, and monitoring the H_2 and HD signal integrals with the experimental scheme shown in Supplementary Fig. 1. Numerical fitting was performed in MATLAB[74], as described in 'Fitting of Enzyme kinetics' in Supplementary Discussion, assuming the kinetic model shown in Supplementary Fig. 17.

To obtain restraints for the kinetic parameters in the model with two bound states (Fig. 7a) from the kinetic parameters fitted to the model with one bound state (Fig. 2c and Supplementary Fig. 17), steady-state analysis of simplified kinetic models (Supplementary Fig. 18) was performed (Supplementary Discussion).

Simulation of NMR spectra and PHIP-CEST curves

Nuclear spin dynamics calculations were performed in MATLAB[74], using the MOIN spin simulation library[75]. The details of the simulations (equations and explanatory illustrations) are given in the Supplementary Discussion (sections 'Spin Dynamics Models for Numerical Simulations' through 'Simulation of PHIP-CEST curves'). Chemical kinetics models assumed for numerical simulations are graphically summarized in Supplementary Fig. 22. Simulation parameters used are summarized in Supplementary Tables 9–12 or provided within the corresponding figures and tables.

For fitting the manual field-cycling data (Supplementary Fig. 23b), an analytical description of the simplified kinetic model in Supplementary Fig. 21 was derived (Supplementary Discussion).

Structural modelling and chemical shift calculation

Chemical shifts and J-couplings were computed for a series of QM/MM models derived from two different sources: first, QM/MM models were constructed based on the high-resolution closed-conformation crystal structure (PDB: 6hav) published in ref. 29. Second, the QM/MM models published in figures 9 and 11 of ref. 35, which are derived from molecular dynamics (MD) simulation snapshots, were used, which were kindly supplied by the authors. The QM/MM models from both sources were (re)optimized and used to construct a series of possible hydrogen-bound intermediates of the Hmd active site (Supplementary Tables 13–16).

The QM region used is sketched in Supplementary Fig. 38. It includes the FeGP cofactor up to the phosphate linker, the side chain of Cys176 coordinating to Fe of FeGP, the pterin, imidazoline and phenyl part of the methenyl-H_4MPT^+/methylene-H_4MPT, as well as the hydrogens originating from H_2, which are modelled into the active site. This equals the QM region previously used in ref. 35. For the models based on the crystal structure (models E and G), the His14 residue was included into the QM region due to the close proximity of the N_ε of this residue to the oxygen at the 2-oxypyridine position of FeGP (3.3 Å).

The active region for geometry optimization was built around the Fe centre. It includes all atoms that have a distance of less than 5 Å to the iron centre of FeGP, plus the backbone or side chain (for proteic residues) or full molecules (for non-proteic groups) that these atoms belong to. For the crystal structure-derived models E and G, this includes full molecules of FeGP, methenyl-/methylene-H_4MPT and waters Wat598 and Wat731; the full residues of Cys176, Pro202, Val205 and Pro206; and the side chain atoms of His14, Trp148 and His201. For the MD-derived models A and C, this includes the full molecules of FeGP, methenyl-/methylene-H_4MPT and waters Wat1344 and Wat1070; the full residues of Pro202 and Val205; and the side chain atoms of Trp148, Cys176 and His201.

QM/MM calculations were carried out using the ORCA software[76]. ORCA's default QM/MM settings were used: additive QM/MM with electrostatic embedding[77], link atom approach and using the charge shifting scheme[78] to avoid overpolarization of the electron density at the QM/MM boundary. For the MM, part of the AMBER topology published in ref. 35 was used for models A and C, and was prepared using the open forcefield toolkit for models D to G (after conversion to the prms format as required by the ORCA software using the orca_mm module).

During geometry optimization, only the atomic positions of the active region were optimized, while the positions of all other atoms were kept frozen. The TPSS (Tao, Perdew, Staroverov and Scuseria) density functional[79] together with Grimme's D3BJ dispersion correction[80,81] was used in conjunction with the def2-TZVP basis set[82] and the def2/J auxiliary basis[83].

NMR shielding calculations were performed at the density functional theory level[84], using the TPSS functional[79], the pcSseg-2 basis set[85] (abbreviated to 'pS2' below) and the def2/JK auxiliary basis[83]. Only atoms in the QM region were treated at this level, while the MM region was included as point charges. The ^1H chemical shifts were calculated with respect to tetramethylsilane, whose geometry was optimized at the TPSS-D3BJ/def2-TZVP/CPCM(water) level and NMR shieldings calculated at the TPSS/pS2/CPCM(water) level. Gauge-including atomic orbitals were employed in all shielding calculations and the ad hoc gauge-invariant treatment of the kinetic energy density τ was used (ORCA keyword 'Tau=GI')[86].

Indirect nuclear spin–spin coupling constants were calculated using the PBE0 hybrid functional[87] and the pcJ-2 basis set[88] (abbreviated to 'pJ2' below), together with the def2-TZVPP basis set[82] for Fe. The isotropic parts of the full coupling tensors are reported as scalar J-couplings. Once again, electrostatic QM/MM embedding was applied. All contributions to the spin–spin coupling (Fermi contact, spin–dipole, diamagnetic and paramagnetic spin orbit) were included in the calculations.

To gauge the uncertainty of the calculated NMR properties, several calculations using different density functionals, basis sets and treatments of the environment on a few arbitrarily chosen models were performed, as described in Supplementary Discussion 'NMR parameter calculations: accuracy benchmark' (Supplementary Tables 17–20).

Constrained relaxed surface scans (Supplementary Figs. 41 and 42) were performed as described in Supplementary Methods.

Estimation of magnetic field alignment

Effects of self-alignment of Hmd in the magnetic fields and the resulting RDCs were estimated, as described in Supplementary Methods.

Reporting summary

Further information on research design is available in the Nature Portfolio Reporting Summary linked to this article.

Data availability

The data supporting findings of this study are available within the paper and its Supplementary Information, or from the authors on reasonable request. The crystal structures of closed state jHmd (6hav) was downloaded from the RSCB Protein Data Bank (www.rcsb.org/). QM/MM-optimized structures and NMR parameter computation outputs are available in Supplementary Data 1.

References

1. Yue, M. et al. Hydrogen energy systems: a critical review of technologies, applications, trends and challenges. *Renew. Sustain. Energy Rev.* **146**, 111180 (2021).

2. Zhu, J., Hu, L., Zhao, P., Lee, L. Y. S. & Wong, K.-Y. Recent advances in electrocatalytic hydrogen evolution using nanoparticles. *Chem. Rev.* **120**, 851–918 (2020).
3. Zou, X. & Zhang, Y. Noble metal-free hydrogen evolution catalysts for water splitting. *Chem. Soc. Rev.* **44**, 5148–5180 (2015).
4. Strmcnik, D., Lopes, P. P., Genorio, B., Stamenkovic, V. R. & Markovic, N. M. Design principles for hydrogen evolution reaction catalyst materials. *Nano Energy* **29**, 29–36 (2016).
5. Vignais, P. M. & Billoud, B. Occurrence, classification, and biological function of hydrogenases: an overview. *Chem. Rev.* **107**, 4206–4272 (2007).
6. Peters, J. W. et al. [FeFe]- and [NiFe]-hydrogenase diversity, mechanism, and maturation. *Biochim. Biophys. Acta* **1853**, 1350–1369 (2015).
7. Thauer, R. K., Kaster, A.-K., Seedorf, H., Buckel, W. & Hedderich, R. Methanogenic archaea: ecologically relevant differences in energy conservation. *Nat. Rev. Microbiol.* **6**, 579–591 (2008).
8. Morra, S. Fantastic [FeFe]-hydrogenases and where to find them. *Front. Microbiol.* **13**, 853626 (2022).
9. Lubitz, W., Ogata, H., Rüdiger, O. & Reijerse, E. Hydrogenases. *Chem. Rev.* **114**, 4081–4148 (2014).
10. Vincent, K. A., Parkin, A. & Armstrong, F. A. Investigating and exploiting the electrocatalytic properties of hydrogenases. *Chem. Rev.* **107**, 4366–4413 (2007).
11. Ghimire, A. et al. A review on dark fermentative biohydrogen production from organic biomass: process parameters and use of by-products. *Appl. Energy* **144**, 73–95 (2015).
12. Cao, Y., Liu, H., Liu, W., Guo, J. & Xian, M. Debottlenecking the biological hydrogen production pathway of dark fermentation: insight into the impact of strain improvement. *Microb. Cell Fact.* **21**, 166 (2022).
13. Evans, R. M. et al. The value of enzymes in solar fuels research—efficient electrocatalysts through evolution. *Chem. Soc. Rev.* **48**, 2039–2052 (2019).
14. Xu, Z. et al. Photosynthetic hydrogen production by droplet-based microbial micro-reactors under aerobic conditions. *Nat. Commun.* **11**, 5985 (2020).
15. Fang, X., Kalathil, S. & Reisner, E. Semi-biological approaches to solar-to-chemical conversion. *Chem. Soc. Rev.* **49**, 4926–4952 (2020).
16. Morra, S., Valetti, F. & Gilardi, G. [FeFe]-hydrogenases as biocatalysts in bio-hydrogen production. *Rend. Lincei Sci. Fis. Nat.* **28**, 183–194 (2017).
17. Hwang, J.-H. et al. Photoautotrophic hydrogen production by eukaryotic microalgae under aerobic conditions. *Nat. Commun.* **5**, 3234 (2014).
18. Appel, J., Hueren, V., Boehm, M. & Gutekunst, K. Cyanobacterial in vivo solar hydrogen production using a photosystem I–hydrogenase (PsaD–HoxYH) fusion complex. *Nat. Energy* **5**, 458–467 (2020).
19. Kanygin, A. et al. Rewiring photosynthesis: a photosystem I–hydrogenase chimera that makes H_2 in vivo. *Energy Environ. Sci.* **13**, 2903–2914 (2020).
20. Zirngibl, C. et al.H_2-forming methylenetetrahydromethanopterin dehydrogenase, a novel type of hydrogenase without iron–sulfur clusters in methanogenic archaea. *Eur. J. Biochem.* **208**, 511–520 (1992).
21. Best, S. P. Spectroelectrochemistry of hydrogenase enzymes and related compounds. *Coord. Chem. Rev.* **249**, 1536–1554 (2005).
22. Stripp, S. T. In situ infrared spectroscopy for the analysis of gas-processing metalloenzymes. *ACS Catal.* **11**, 7845–7862 (2021).
23. Fan, C. et al. Detection and characterization of exchangeable protons bound to the hydrogen-activation nickel site of *Desulfovibrio gigas* hydrogenase: a proton and deuterium Q-band ENDOR study. *J. Am. Chem. Soc.* **113**, 20–24 (1991).
24. Foerster, S. et al. Single crystal EPR studies of the reduced active site of [NiFe] hydrogenase from *Desulfovibrio vulgaris* Miyazaki F. *J. Am. Chem. Soc.* **125**, 83–93 (2003).
25. Ogata, H., Nishikawa, K. & Lubitz, W. Hydrogens detected by subatomic resolution protein crystallography in a [NiFe] hydrogenase. *Nature* **520**, 571–574 (2015).
26. Ogata, H. et al. Hydride bridge in [NiFe]-hydrogenase observed by nuclear resonance vibrational spectroscopy. *Nat. Commun.* **6**, 7890 (2015).
27. Reijerse, E. J. et al. Direct observation of an iron-bound terminal hydride in [FeFe]-hydrogenase by nuclear resonance vibrational spectroscopy. *J. Am. Chem. Soc.* **139**, 4306–4309 (2017).
28. Rumpel, S., Sommer, C., Reijerse, E., Farès, C. & Lubitz, W. Direct detection of the terminal hydride intermediate in [FeFe] hydrogenase by NMR spectroscopy. *J. Am. Chem. Soc.* **140**, 3863–3866 (2018).
29. Huang, G. et al. The atomic-resolution crystal structure of activated [Fe]-hydrogenase. *Nat. Catal.* **2**, 537–543 (2019).
30. Shima, S. et al. The crystal structure of [Fe]-hydrogenase reveals the geometry of the active site. *Science* **321**, 572–575 (2008).
31. Hiromoto, T. et al. The crystal structure of C176A mutated [Fe]-hydrogenase suggests an acyl-iron ligation in the active site iron complex. *FEBS Lett.* **583**, 585–590 (2009).
32. Schleucher, J., Griesinger, C., Schwörer, B. & Thauer, R. K. H_2-forming N_5,N_{10}-methylenetetrahydromethanopterin dehydrogenase from *Methanobacterium thermoautotrophicum* catalyzes a stereoselective hydride transfer as determined by two-dimensional NMR spectroscopy. *Biochem* **33**, 3986–3993 (1994).
33. Schwörer, B., Fernandez, V. M., Zirngibl, C. & Thauer, R. K. H_2-forming N5,N10-methylenetetrahydromethanopterin dehydrogenase from Methanobacterium thermoautotrophicum. Studies of the catalytic mechanism of H_2 formation using hydrogen isotopes. *Eur. J. Biochem.* **212**, 255–261 (1993).
34. Yang, X. & Hall, M. B. Monoiron hydrogenase catalysis: hydrogen activation with the formation of a dihydrogen, $Fe^{-}H\delta^{-}\cdots H\delta^{+}-O$, bond and methenyl-$H_4MPT^{+}$ triggered hydride transfer. *J. Am. Chem. Soc.* **131**, 10901–10908 (2009).
35. Finkelmann, A. R., Senn, H. M. & Reiher, M. Hydrogen-activation mechanism of [Fe] hydrogenase revealed by multi-scale modeling. *Chem. Sci.* **5**, 4474–4482 (2014).
36. Shima, S., Lyon, E. J., Thauer, R. K., Mienert, B. & Bill, E. Mössbauer studies of the iron–sulfur cluster-free hydrogenase: the electronic state of the mononuclear Fe active site. *J. Am. Chem. Soc.* **127**, 10430–10435 (2005).
37. Lyon, E. J. et al. Carbon monoxide as an intrinsic ligand to iron in the active site of the iron–sulfur-cluster-free hydrogenase H_2-forming methylenetetrahydromethanopterin dehydrogenase as revealed by infrared spectroscopy. *J. Am. Chem. Soc.* **126**, 14239–14248 (2004).
38. Korbas, M. et al. The iron-sulfur cluster-free hydrogenase (Hmd) is a metalloenzyme with a novel iron binding motif. *J. Biol. Chem.* **281**, 30804–30813 (2006).
39. Schleucher, J., Schwörer, B., Thauer, R. K. & Griesinger, C. Elucidation of the stereochemical course of chemical reactions by magnetic labeling. *J. Am. Chem. Soc.* **117**, 2941–2942 (1995).
40. Bowers, C. R. & Weitekamp, D. P. Transformation of symmetrization order to nuclear-spin magnetization by chemical reaction and nuclear magnetic resonance. *Phys. Rev. Lett.* **57**, 2645–2648 (1986).
41. Eisenschmid, T. C. et al. Para hydrogen induced polarization in hydrogenation reactions. *J. Am. Chem. Soc.* **109**, 8089–8091 (1987).
42. Pravica, M. G. & Weitekamp, D. P. Net NMR alignment by adiabatic transport of parahydrogen addition products to high magnetic field. *Chem. Phys. Lett.* **145**, 255–258 (1988).

43. Natterer, J. & Bargon, J. Parahydrogen induced polarization. *Prog. Nucl. Magn. Reson. Spectrosc.* **31**, 293–315 (1997).
44. Buntkowsky, G. & Gutmann, T. PASADENA NMR. *Nat. Catal.* **5**, 848–849 (2022).
45. Duckett, S. B. & Sleigh, C. J. Applications of the parahydrogen phenomenon: a chemical perspective. *Prog. Nucl. Magn. Reson. Spectrosc.* **34**, 71–92 (1999).
46. Godard, C., Duckett, S. B., Polas, S., Tooze, R. & Whitwood, A. C. Detection of intermediates in cobalt-catalyzed hydroformylation using para-hydrogen-induced polarization. *J. Am. Chem. Soc.* **127**, 4994–4995 (2005).
47. Zakharov, D. O. et al. Parahydrogen-induced polarization in hydrogenation reactions mediated by a metal-free catalyst. *Chem. Eur. J.* **28**, e202103501 (2022).
48. Kiryutin, A. S. et al. Parahydrogen allows ultrasensitive indirect NMR detection of catalytic hydrogen complexes. *J. Phys. Chem. C.* **121**, 9879–9888 (2017).
49. Parastaev, A. et al. Breaking structure sensitivity in CO_2 hydrogenation by tuning metal–oxide interfaces in supported cobalt nanoparticles. *Nat. Catal.* **5**, 1051–1060 (2022).
50. Chen, S. et al. Ultrasmall amorphous zirconia nanoparticles catalyse polyolefin hydrogenolysis. *Nat. Catal.* **6**, 161–173 (2023).
51. Permin, A. B. & Eisenberg, R. One-hydrogen polarization in hydroformylation promoted by platinum–tin and iridium carbonyl complexes: a new type of parahydrogen-induced effect. *J. Am. Chem. Soc.* **124**, 12406–12407 (2002).
52. Glöggler, S. et al. Para-hydrogen induced polarization of amino acids, peptides and deuterium-hydrogen gas. *Phys. Chem. Chem. Phys.* **13**, 13759–13764 (2011).
53. Lehmkuhl, S. et al. Hyperpolarizing water with parahydrogen. *ChemPhysChem* **18**, 2426–2429 (2017).
54. Emondts, M., Schikowski, D., Klankermayer, J. & Schleker, P. P. M. Non-pairwise interactions in parahydrogen experiments: nuclear exchange of single protons enables bulk water hyperpolarization. *ChemPhysChem* **19**, 2614–2620 (2018).
55. Luther, T. A. & Heinekey, D. M. Determination of the H–H distance in transition-metal dihydrogen complexes: effects of high magnetic fields. *J. Am. Chem. Soc.* **119**, 6688–6689 (1997).
56. Lisicki, M. A., Mishra, P. K., Bothner-By, A. A. & Lindsey, J. S. Solution conformation of a porphyrin-quinone cage molecule determined by dipolar magnetic field effects in ultra-high-field NMR. *J. Phys. Chem.* **92**, 3400–3403 (1988).
57. Tolman, J. R., Flanagan, J. M., Kennedy, M. A. & Prestegard, J. H. Nuclear magnetic dipole interactions in field-oriented proteins: information for structure determination in solution. *Proc. Natl Acad. Sci. USA* **92**, 9279–9283 (1995).
58. Zhao, E. W. et al. Surface-mediated hyperpolarization of liquid water from parahydrogen. *Chem* **4**, 1387–1403 (2018).
59. Geierstanger, B. H. et al. Catalytic mechanism of the metal-free hydrogenase from methanogenic archaea: reversed stereospecificity of the catalytic and noncatalytic reaction. *Angew. Chem. Int. Ed.* **37**, 3300–3303 (1998).
60. Escalante-Semerena, J. C., Rinehart, K. L. Jr & Wolfe, R. S. Tetrahydromethanopterin, a carbon carrier in methanogenesis. *J. Biol. Chem.* **259**, 9447–9455 (1984).
61. Leroux, F. et al. Experimental approaches to kinetics of gas diffusion in hydrogenase. *Proc. Natl Acad. Sci. USA* **105**, 11188–11193 (2008).
62. Pilak, O. et al. The crystal structure of the apoenzyme of the iron–sulphur cluster-free hydrogenase. *J. Mol. Biol.* **358**, 798–809 (2006).
63. Eckert, J., Kubas, G. J., Hall, J. H., Hay, P. J. & Boyle, C. M. Molecular hydrogen complexes. 6. The barrier to rotation of η^2-H_2 in $M(CO)_3(PR3)_2(\eta^2\text{-}H_2)$ (M = tungsten, molybdenum; R = cyclohexyl, isopropyl): inelastic neutron scattering, theoretical, and molecular mechanics studies. *J. Am. Chem. Soc.* **112**, 2324–2332 (1990).
64. Maltby, P. A. et al. Dihydrogen with frequency of motion near the ^{1}H Larmor frequency. Solid-state structures and solution NMR spectroscopy of osmium complexes *trans*-$[Os(H{\cdot\cdot}H)X(PPh_2CH_2CH_2PPh_2)_2]^+$ (X = Cl, Br). *J. Am. Chem. Soc.* **118**, 5396–5407 (1996).
65. Limbach, H.-H. et al. NMR and INS line shapes of transition metal hydrides in the presence of coherent and incoherent dihydrogen exchange. *J. Am. Chem. Soc.* **120**, 7929–7943 (1998).
66. Klein, A. R., Hartmann, G. C. & Thauer, R. K. Hydrogen isotope effects in the reactions catalyzed by H_2-forming N_5,N_{10}-methylenetetrahydromethanopterin dehydrogenase from methanogenic archaea. *Eur. J. Biochem.* **233**, 372–376 (1995).
67. Forsén, S. & Hoffman, R. A. Study of moderately rapid chemical exchange reactions by means of nuclear magnetic double resonance. *J. Chem. Phys.* **39**, 2892–2901 (2004).
68. Palmer, A. G. & Koss, H. in *Methods Enzymol.* vVol. 615 (ed. Joshua Wand, A.) 177–236 (Academic, 2019).
69. Vallurupalli, P., Bouvignies, G. & Kay, L. E. Studying 'invisible' excited protein states in slow exchange with a major state conformation. *J. Am. Chem. Soc.* **134**, 8148–8161 (2012).
70. Schröder, L., Lowery, T. J., Hilty, C., Wemmer, D. E. & Pines, A. Molecular imaging using a targeted magnetic resonance hyperpolarized biosensor. *Science* **314**, 446–449 (2006).
71. Bowers, C. R. & Weitekamp, D. P. Parahydrogen and synthesis allow dramatically enhanced nuclear alignment. *J. Am. Chem. Soc.* **109**, 5541–5542 (1987).
72. Schönheit, P., Moll, J. & Thauer, R. K. Growth parameters (K_s, μ_{max}, Y_s) of *Methanobacterium thermoautotrophicum*. *Arch. Microbiol.* **127**, 59–65 (1980).
73. Moore, J. T., Uppal, A., Maley, F. & Maley, G. F. Overcoming inclusion body formation in a high-level expression system. *Protein Expr. Purif.* **4**, 160–163 (1993).
74. MATLAB v. 9.9.0.1467703 (R2020b) (MathWorks, 2020).
75. Pravdivtsev, A. N. & Hövener, J.-B. Simulating non-linear chemical and physical (CAP) dynamics of signal amplification by reversible exchange (SABRE). *Chem. Eur. J.* **25**, 7659–7668 (2019).
76. Neese, F. Software update: the ORCA program system—version 5.0. *Wiley Interdiscip. Rev. Comput. Mol. Sci.* **12**, e1606 (2022).
77. Senn, H. M. & Thiel, W. in *Atomistic Approaches in Modern Biology: from Quantum Chemistry to Molecular Simulations* (ed. Reiher, M.) 173–290 (Springer, 2007).
78. Lin, H. & Truhlar, D. G. Redistributed charge and dipole schemes for combined quantum mechanical and molecular mechanical calculations. *J. Phys. Chem. A* **109**, 3991–4004 (2005).
79. Tao, J., Perdew, J. P., Staroverov, V. N. & Scuseria, G. E. Climbing the density functional ladder: nonempirical meta–generalized gradient approximation designed for molecules and solids. *Phys. Rev. Lett.* **91**, 146401 (2003).
80. Grimme, S., Antony, J., Ehrlich, S. & Krieg, H. A consistent and accurate ab initio parametrization of density functional dispersion correction (DFT-D) for the 94 elements H-Pu. *J. Chem. Phys.* **132**, 154104 (2010).
81. Grimme, S., Ehrlich, S. & Goerigk, L. Effect of the damping function in dispersion corrected density functional theory. *J. Comput. Chem.* **32**, 1456–1465 (2011).
82. Weigend, F. & Ahlrichs, R. Balanced basis sets of split valence, triple zeta valence and quadruple zeta valence quality for H to Rn: design and assessment of accuracy. *Phys. Chem. Chem. Phys.* **7**, 3297–3305 (2005).
83. Weigend, F. Hartree–Fock exchange fitting basis sets for H to Rn †. *J. Comput. Chem.* **29**, 167–175 (2008).
84. Stoychev, G. L., Auer, A. A., Izsák, R. & Neese, F. Self-consistent field calculation of nuclear magnetic resonance chemical shielding constants using gauge-including atomic orbitals and approximate two-electron integrals. *J. Chem. Theory Comput.* **14**, 619–637 (2018).

85. Jensen, F. Segmented contracted basis sets optimized for nuclear magnetic shielding. *J. Chem. Theory Comput.* **11**, 132–138 (2015).
86. Schattenberg, C. J. & Kaupp, M. Effect of the current dependence of tau-dependent exchange-correlation functionals on nuclear shielding calculations. *J. Chem. Theory Comput.* **17**, 1469–1479 (2021).
87. Adamo, C. & Barone, V. Toward reliable density functional methods without adjustable parameters: the PBE0 model. *J. Chem. Phys.* **110**, 6158–6170 (1999).
88. Jensen, F. The basis set convergence of spin–spin coupling constants calculated by density functional methods. *J. Chem. Theory Comput.* **2**, 1360–1369 (2006).

Acknowledgements

We thank M. Reiher and M. Woodrich for providing the structural models for Hmd published in ref. 35 and ref. 29, respectively, and for helpful discussions. We thank D. Becker and A. Dressler for feedback on the paper and editing. The following funding is acknowledged: Max Planck Society (L.K., M.K., M.G., G.H., G.L.S., F.N., A.A.A., C.G., S.S. and S.G). German Research Foundation (DFG) grants SPP 1927: SH 87/1-1 and SH 87/1-2 (S.S.) and grants PR 1868/3-1, HO-4602/2-2, HO-4602/3, GRK2154-2019, EXC2167, FOR5042, SFB1479 and TRR287 (A.N.P. and J.-B.H.). The German Federal Ministry of Education and Research (BMBF), framework of the e:Med research and funding concept (01ZX1915C) (A.N.P.), the European Regional Development Fund (J.-B.H.) and Zukunftsprogramm Wirtschaft of Schleswig-Holstein (project no. 122-09-053) (J.-B.H.)

Author contributions

C.G., A.N.P., S.G. and S.S. initially conceived the work. M.G. and G.H. performed protein and cofactor preparation. NMR experiments were designed by L.K., A.N.P., C.G. and S.G. L.K. performed NMR experiments, data analysis and visualization thereof. A.N.P., L.K. and M.K. performed kinetics and spin dynamics modelling. C.R., G.L.S., F.N. and A.A.A. performed structural modelling and δ and J computations. All authors contributed to data interpretation. L.K. prepared the initial manuscript with contributions from M.G., S.G., M.K. and A.N.P. and all authors contributed to its revision.

Funding

Open access funding provided by Max Planck Society.

Competing interests

The authors declare no competing interests.

Additional information

Supplementary information The online version contains supplementary material available at https://doi.org/10.1038/s41929-024-01262-w.

Correspondence and requests for materials should be addressed to Christian Griesinger, Seigo Shima or Stefan Glöggler.

Peer review information *Nature Catalysis* thanks Clifford Bowers, Sven Stripp and the other, anonymous, reviewer(s) for their contribution to the peer review of this work.

Reprints and permissions information is available at www.nature.com/reprints.

Publisher's note Springer Nature remains neutral with regard to jurisdictional claims in published maps and institutional affiliations.

Open Access This article is licensed under a Creative Commons Attribution 4.0 International License, which permits use, sharing, adaptation, distribution and reproduction in any medium or format, as long as you give appropriate credit to the original author(s) and the source, provide a link to the Creative Commons licence, and indicate if changes were made. The images or other third party material in this article are included in the article's Creative Commons licence, unless indicated otherwise in a credit line to the material. If material is not included in the article's Creative Commons licence and your intended use is not permitted by statutory regulation or exceeds the permitted use, you will need to obtain permission directly from the copyright holder. To view a copy of this licence, visit http://creativecommons.org/licenses/by/4.0/.

© The Author(s) 2024

nature portfolio

Corresponding author(s): Christian Griesinger, Seigo Shima, Stefan Glöggler

Last updated by author(s): 16.10.2024

Reporting Summary

Nature Portfolio wishes to improve the reproducibility of the work that we publish. This form provides structure for consistency and transparency in reporting. For further information on Nature Portfolio policies, see our Editorial Policies and the Editorial Policy Checklist.

Please do not complete any field with "not applicable" or n/a. Refer to the help text for what text to use if an item is not relevant to your study.
For final submission: please carefully check your responses for accuracy; you will not be able to make changes later.

Statistics

For all statistical analyses, confirm that the following items are present in the figure legend, table legend, main text, or Methods section.

n/a	Confirmed	
☐	☒	The exact sample size (*n*) for each experimental group/condition, given as a discrete number and unit of measurement
☐	☒	A statement on whether measurements were taken from distinct samples or whether the same sample was measured repeatedly
☒	☐	The statistical test(s) used AND whether they are one- or two-sided *Only common tests should be described solely by name; describe more complex techniques in the Methods section.*
☒	☐	A description of all covariates tested
☒	☐	A description of any assumptions or corrections, such as tests of normality and adjustment for multiple comparisons
☐	☒	A full description of the statistical parameters including central tendency (e.g. means) or other basic estimates (e.g. regression coefficient) AND variation (e.g. standard deviation) or associated estimates of uncertainty (e.g. confidence intervals)
☒	☐	For null hypothesis testing, the test statistic (e.g. *F*, *t*, *r*) with confidence intervals, effect sizes, degrees of freedom and *P* value noted *Give P values as exact values whenever suitable.*
☒	☐	For Bayesian analysis, information on the choice of priors and Markov chain Monte Carlo settings
☒	☐	For hierarchical and complex designs, identification of the appropriate level for tests and full reporting of outcomes
☒	☐	Estimates of effect sizes (e.g. Cohen's *d*, Pearson's *r*), indicating how they were calculated

Our web collection on statistics for biologists contains articles on many of the points above.

Software and code

Policy information about availability of computer code

Data collection	Topspin 3.6 patchlevel 2 (experiments at 14.1T), Topspin 3.5 patchlevel 7 (experiments at 21.15T and 7.05 T narrow bore system) and TopSpin 4.0 patchlevel 7 (for experiments at 7.05 T widebore system)
Data analysis	Matlab R2020b; using the MOIN spin simulation library, ORCA software package, version 5.0, revision 20216; Topspin 4.0 patchlevel 6; Igor Pro 6.3.7.2 (WaveMetrics, Inc.) UCSF Chimera 1.14

For manuscripts utilizing custom algorithms or software that are central to the research but not yet described in published literature, software must be made available to editors and reviewers. We strongly encourage code deposition in a community repository (e.g. GitHub). See the Nature Portfolio guidelines for submitting code & software for further information.

Data

Policy information about availability of data

All manuscripts must include a data availability statement. This statement should provide the following information, where applicable:

- Accession codes, unique identifiers, or web links for publicly available datasets
- A description of any restrictions on data availability
- For clinical datasets or third party data, please ensure that the statement adheres to our policy

The following statement was added:
The data supporting findings of this study are available within the paper and its Supplementary Information, or from the authors on reasonable request. The crystal structures of closed state jHmd (6hav) was downloaded from the RSCB Protein Data Bank (www.rcsb.org/). QM/MM-optimized structures and NMR parameter computation outputs are available in Supplementary data 1.

Research involving human participants, their data, or biological material

Policy information about studies with human participants or human data. See also policy information about sex, gender (identity/presentation), and sexual orientation and race, ethnicity and racism.

Reporting on sex and gender	N/A
Reporting on race, ethnicity, or other socially relevant groupings	N/A
Population characteristics	N/A
Recruitment	N/A
Ethics oversight	N/A

Note that full information on the approval of the study protocol must also be provided in the manuscript.

Field-specific reporting

Please select the one below that is the best fit for your research. If you are not sure, read the appropriate sections before making your selection.

☒ Life sciences ☐ Behavioural & social sciences ☐ Ecological, evolutionary & environmental sciences

For a reference copy of the document with all sections, see nature.com/documents/nr-reporting-summary-flat.pdf

Life sciences study design

All studies must disclose on these points even when the disclosure is negative.

Sample size	No sample size calculation
Data exclusions	No data excluded
Replication	Not applicable
Randomization	Not applicable
Blinding	Not applicable

Behavioural & social sciences study design

All studies must disclose on these points even when the disclosure is negative.

Study description	
Research sample	
Sampling strategy	
Data collection	
Timing	
Data exclusions	
Non-participation	
Randomization	

Ecological, evolutionary & environmental sciences study design

All studies must disclose on these points even when the disclosure is negative.

Study description	
Research sample	
Sampling strategy	
Data collection	
Timing and spatial scale	
Data exclusions	
Reproducibility	
Randomization	
Blinding	

Did the study involve field work? ☐ Yes ☐ No

Field work, collection and transport

Field conditions	
Location	
Access & import/export	
Disturbance	

Reporting for specific materials, systems and methods

We require information from authors about some types of materials, experimental systems and methods used in many studies. Here, indicate whether each material, system or method listed is relevant to your study. If you are not sure if a list item applies to your research, read the appropriate section before selecting a response.

Materials & experimental systems

n/a	Involved in the study
☒	☐ Antibodies
☒	☐ Eukaryotic cell lines
☒	☐ Palaeontology and archaeology
☒	☐ Animals and other organisms
☒	☐ Clinical data
☒	☐ Dual use research of concern
☒	☐ Plants

Methods

n/a	Involved in the study
☒	☐ ChIP-seq
☒	☐ Flow cytometry
☒	☐ MRI-based neuroimaging

Antibodies

Antibodies used	
Validation	

Eukaryotic cell lines

Policy information about cell lines and Sex and Gender in Research

Cell line source(s)	
Authentication	
Mycoplasma contamination	
Commonly misidentified lines (See ICLAC register)	

Palaeontology and Archaeology

Specimen provenance	
Specimen deposition	
Dating methods	

☐ Tick this box to confirm that the raw and calibrated dates are available in the paper or in Supplementary Information.

Ethics oversight	

Note that full information on the approval of the study protocol must also be provided in the manuscript.

Animals and other research organisms

Policy information about studies involving animals; ARRIVE guidelines recommended for reporting animal research, and Sex and Gender in Research

Laboratory animals	
Wild animals	
Reporting on sex	
Field-collected samples	
Ethics oversight	

Note that full information on the approval of the study protocol must also be provided in the manuscript.

Clinical data

Policy information about clinical studies

All manuscripts should comply with the ICMJE guidelines for publication of clinical research and a completed CONSORT checklist must be included with all submissions.

Clinical trial registration	
Study protocol	
Data collection	
Outcomes	

Dual use research of concern

Policy information about dual use research of concern

Hazards

Could the accidental, deliberate or reckless misuse of agents or technologies generated in the work, or the application of information presented in the manuscript, pose a threat to:

No	Yes	
☒	☐	Public health
☒	☐	National security
☒	☐	Crops and/or livestock
☒	☐	Ecosystems
☒	☐	Any other significant area

Experiments of concern

Does the work involve any of these experiments of concern:

No	Yes	
☒	☐	Demonstrate how to render a vaccine ineffective
☒	☐	Confer resistance to therapeutically useful antibiotics or antiviral agents
☒	☐	Enhance the virulence of a pathogen or render a nonpathogen virulent
☒	☐	Increase transmissibility of a pathogen
☒	☐	Alter the host range of a pathogen
☒	☐	Enable evasion of diagnostic/detection modalities
☒	☐	Enable the weaponization of a biological agent or toxin
☒	☐	Any other potentially harmful combination of experiments and agents

Plants

Seed stocks

Novel plant genotypes

Authentication

ChIP-seq

Data deposition

☐ Confirm that both raw and final processed data have been deposited in a public database such as GEO.

☐ Confirm that you have deposited or provided access to graph files (e.g. BED files) for the called peaks.

Data access links
May remain private before publication.

Files in database submission

Genome browser session
(e.g. UCSC)

Methodology

Replicates

Sequencing depth

Antibodies

Peak calling parameters

Data quality

Software

Flow Cytometry

Plots

Confirm that:

☐ The axis labels state the marker and fluorochrome used (e.g. CD4-FITC).

☐ The axis scales are clearly visible. Include numbers along axes only for bottom left plot of group (a 'group' is an analysis of identical markers).

☐ All plots are contour plots with outliers or pseudocolor plots.

☐ A numerical value for number of cells or percentage (with statistics) is provided.

Methodology

Sample preparation

Instrument

Software

Cell population abundance

Gating strategy

☐ Tick this box to confirm that a figure exemplifying the gating strategy is provided in the Supplementary Information.

Magnetic resonance imaging

Experimental design

Design type

Design specifications

Behavioral performance measures

Imaging type(s)

Field strength

Sequence & imaging parameters

Area of acquisition

Diffusion MRI ☐ Used ☐ Not used

Preprocessing

Preprocessing software

Normalization

Normalization template

Noise and artifact removal

Volume censoring

Statistical modeling & inference

Model type and settings

Effect(s) tested

Specify type of analysis: ☐ Whole brain ☐ ROI-based ☐ Both

Statistic type for inference

(See Eklund et al. 2016)

Correction

Models & analysis

n/a	Involved in the study
☒	☐ Functional and/or effective connectivity
☒	☐ Graph analysis
☒	☐ Multivariate modeling or predictive analysis

Functional and/or effective connectivity

Graph analysis

Multivariate modeling and predictive analysis

This checklist template is licensed under a Creative Commons Attribution 4.0 International License, which permits use, sharing, adaptation, distribution and reproduction in any medium or format, as long as you give appropriate credit to the original author(s) and the source, provide a link to the Creative Commons license, and indicate if changes were made. The images or other third party material in this article are included in the article's Creative Commons license, unless indicated otherwise in a credit line to the material. If material is not included in the article's Creative Commons license and your intended use is not permitted by statutory regulation or exceeds the permitted use, you will need to obtain permission directly from the copyright holder. To view a copy of this license, visit http://creativecommons.org/licenses/by/4.0/